Supplement of Atmos. Chem. Phys., 26, 15831–15852, 2026
https://doi.org/10.5194/acp-26-15831-2026-supplement
© Author(s) 2026. CC BY 4.0 License.



Atmospheric Chemistry and Physics
Open Access
EGU

*Supplement of*

# The synergy of morphology and mixing state on the absorption of coated black carbon soot

**Johannes Heuser et al.**

*Correspondence to:* Johannes Heuser (hannes.heu@gmail.com) and Claudia Di Biagio (claudia.dibiagio@lisa.ipsl.fr)

The copyright of individual parts of the supplement might differ from the article licence.

## Supporting Information Text

### Sect. S1. Experimental protocol of control experiments

A list of all ageing experiments and control experiments considered in this study is provided in Table 1 in the main manuscript. The control experiments follow the basic principle shown in Table S1. All experiments start with the filling of the chamber, the injection of the soot and its characterization, which are summarized in Heuser et al. (2025). Only after these steps, the ageing part of the experiments begins, which differs for the individual experiments based on the objective of the study. These individual objectives and the necessary protocols used are briefly discussed in the following.

Soot coagulation dry: these experiments aim to investigate the impact the time in suspensions and coagulation has on the soot properties. Two experiments were performed by leaving the soot in suspension for around 24 hours, i.e. the same length as for the long coating experiments. The soot was left in the chamber without any other active processing, and the only injections were the constant addition of $N_2$ and $O_2$ to compensate for the instrumental sampling losses. The soot properties were measured for about the first 8 hours and the last 4 to 6 hours using online measurements and filter samples to characterize soot from the beginning to the end of the experiments. The two experiments were tested at two different soot concentrations to vary the coagulation rate and get information on the impact of stronger and weaker coagulation processes.

Soot coagulation humid: these experiments targeted the investigation of the impact of relative humidity and the injection protocol for water vapor on the soot properties. The humid experiments were performed targeting a relative humidity of around 30% in line with the one used in coating experiments. The properties of the soot in these humid conditions were measured for 5 hours with a set of filter measurements and effective density scans. During this time, as also in other experiments, the water content in the chamber was constantly kept stable between 25-35% by continuously compensating for the water losses due to dilution during experiments.

Soot irradiation dry: the impact of irradiation on the soot aerosol was assessed in two experiments. The three 6.5 kW Xenon arc lamps were used to irradiate the chamber volume, simulating solar radiation, and a cryostat was used throughout irradiation time to minimize the heating effect of the lamps on the chamber volume. During the whole experiment, the soot properties were measured continuously by online techniques, and a set of filters, as well as effective density measurements, were taken towards the end of the 1- to 2-hour-long irradiation period.

Soot irradiation humid: since the coating experiments were performed in humid conditions, the impact of irradiation was also assessed in humid conditions. For this, after the initial fresh soot measurement, water vapor was injected to reach an RH of around 30%. Then the compensation for the loss of water vapor due to sampling was started, and the soot properties in the humid conditions were monitored using the online techniques for about 80 minutes, during which an effective density scan was also made. After the scan, the lamps and the cryostat were turned on, starting the irradiation of the humid soot-filled chamber. In a 3.5-hour-long measurement interval, the physico-chemical properties of the soot were constantly measured, and filters and density measurements were performed in the latter part of this interval while the chamber volume was illuminated.

Soot ozone irradiation dry and humid: with both coating formations studied in this work relying on the presence of ozone, also the impact of ozone and the presence of OH-radicals on the soot properties was investigated. For this, first, water vapor was injected, following the above-discussed principle, as the first step after the initial soot characterization. Then the soot in humid conditions was characterized. After about 60 to 90 minutes, $O_3$ was injected using a BMT ozone generator (BMT 802N, BMT MESSTECHNIK GMBH), and the soot properties, including the effective density, were acquired in the following 80 minutes. After this measurement interval, the lamps and cryostat were turned on, and the photochemical production of OH-radicals and the potential photochemical ageing of soot were started. The lights were kept on for the next 2 to 3 hours, and the soot properties were measured, including by multiple filter samples. This was done in a total of 5 experiments.

**Sect. S2. Coagulation estimations**

Calculations were performed in order to evaluate the effect of coagulation on soot processing and the likely deposition of material on the soot particles.

In order to derive an estimate for the coagulation potential, the possible collisions of particles per unit of time were calculated following (Dahneke, 1983; Fuchs et al., 1965; Otto et al., 1999; Otto and Fissan, 1999; Park et al., 1999; Seinfeld and Pandis, 2016). This rate for two groups of particles i and j with the mobility size $d_i$ and $d_j$ is defined as

$$\frac{dN(t)}{dt} = \beta(d_i, d_j)N(d_i, t)N(d_j, t) \tag{S1}$$

in which $N(d_{i/j}, t)$ is the number of particles of the mobility size $d_i$ and $d_j$ at time t and $\beta(d_i, d_j)$ is the collision kernel of these two particles. The full number of possible collisions is then calculated by integrating S1 over the full range of particle sizes for $d_i$ and $d_j$ and adjusting to only count collisions once, resulting in:

$$\frac{dN(t)}{dt} = \frac{1}{2}\int_{d_{min}}^{d_{max}}\int_{d_{min}}^{d_{max}} \beta(d_i, d_j)N(d_i, t)N(d_j, t)\ dd_i dd_j. \tag{S2}$$

The collision kernel $\beta(d_i, d_j)$ is calculated via:

$$\beta(d_i, d_i) = 2\pi(d_i + d_j)(D_i + D_j)f(Kn) \tag{S3}$$

following (Otto et al., 1999; Otto and Fissan, 1999; Seinfeld and Pandis, 2016) and is dependent on the mobility size $d_i$ and $d_j$ and diffusion coefficients $D_i$ and $D_j$. The latter ones are determined as:

$$D_i = \frac{kTC_c}{3\pi\mu\ d_i} \tag{S4}$$

where $C_c$ is the slip correction factor, $\mu$ is the viscosity of air, $k$ is the Boltzmann constant, and T is the temperature. Since diffusion depends on the flow regime and the particle size distribution, spanning from the diffusion to the transition regime, this is accounted for using a correction function for flow regimes, $f$, calculated as (Dahneke, 1983; Otto et al., 1999):

$$f(Kn) = \frac{1 + Kn}{1 + 2Kn + 2Kn^2} \tag{S5}$$

The Knudsen number of the particles is related to the mean free path $\lambda_P$ of the diffusing particles as:

$$Kn = \frac{2\lambda_P}{d_{ij}}\ with\ \lambda_P = \frac{3(D_i + D_j)}{\bar{c}_{ij}}\ and\ \bar{c}_{ij} = \left(\left(\left(\frac{8kT}{\pi m_i}\right)^{\frac{1}{2}}\right)^2 + \left(\left(\frac{8kT}{\pi m_j}\right)^{\frac{1}{2}}\right)^2\right)^{\frac{1}{2}} \tag{S6}$$

The mass $m_i$ of each aggregate necessary for this calculation was derived using the known mass at each size from the mass-resolved size measurements, used to determine the effective density.

Since these calculations served the aim of providing information on the soot processing, in particular after the formation of nucleated secondary aerosol, calculations were adjusted to isolate the coagulation of soot-containing particles as much as possible. Isolation was achieved by using the different identifiable modes of the aerosol (see Fig. 1 and 2 in the main manuscript and Fig S11 to S16). The modes were used to define a critical diameter $d_{min_{soot}}$, that represents the lower boundary of the size range that is dominated by soot-containing particles, which in turn is used to perform a size-selective calculations.

These size-dependent calculations were further applied, cumulatively integrating over the measurement interval t, allowing for the calculation of a cumulative coagulation that is given as relative to the initial number concentration, $N_0$. The final formulation is as follows:

$$CC(t) = \begin{cases} \dfrac{\int_0^t \int_{d_{min_{soot}}}^{d_{max}} \int_{d_{min}}^{d_{max}} \beta(d_i, d_i) N(d_i, t) N(d_j, t)\ dd_i dd_j dt}{N_0} & if\ d_{min_{soot}} \geq d_{min} \\ \dfrac{\int_0^t \frac{1}{2} \int_{d_{min_{soot}}}^{d_{max}} \int_{d_{min}}^{d_{max}} \beta(d_i, d_i) N(d_i, t) N(d_j, t)\ dd_i dd_j dt}{N_0} & if\ d_{min_{soot}} < d_{min} \end{cases} \quad (S7)$$

The *CC(t)* provides the relative frequency with which the particles of the original number size distribution may have undergone coagulation with soot, soot-containing particles, and/or secondary aerosol particles at any time t after their injection into the chamber.

In addition to the number of particles coagulating, a relative measure was calculated to estimate the soot mass concentration potentially involved in coagulation. Since for each size, both number and effective density are known, a rough estimate of how much mass may coagulate could be made following the same principle as CC(t). In order to compare different experiments, values were normalized using the initial mass concentration, allowing estimation of the relevance of coagulation in the process of mass deposition for the formation process of the coating and during the overnight ageing.

Results of these calculations for the six coating experiments are displayed in Fig. S9 and S10 for $H_2SO_4$ and SOA coating, respectively. Additionally, reference data on coagulation during non-coating experiments is provided. The rates from control experiments are due to the absence of a secondary species, determined without a critical diameter $d_{min_{soot}}$. The best comparison is provided by the long-term ageing experiments of CS1 coagulation dry 1 and 2, which differ in their initial soot concentration. The coagulation dry 1 experiment is comparable in initial concentration to the $S_{ref}$ and $H_2SO_4$ experiments, and coagulation dry 2 to the SOA-$S_{high}$ experiment.

The results for CS1 coagulation dry 1 and 2 show that for pure soot aerosol, the majority of potential coagulation and mass coagulation is likely to occur in the first 1 to 1.5 hours after injection, beyond this the possibility and thus relevance of coagulation reduces significantly. However, potential coagulation remains given throughout the entire lifetime of the soot.

The addition of a secondary phase alters both the number size distribution and the physico-chemical properties of soot. This modification affects the coagulation potential, depending on the properties of the homogeneously nucleated secondary aerosol and the soot-containing particles, which are known to differ between the two coating types.

The $H_2SO_4$ generation produces larger secondary particles with CMD diameters of the secondary aerosol due to processing growing close to the CMD of the soot-containing particles. For these, a significant increase in potential coagulation rate can be observed. Similar to the soot injection, the absolute majority of this potential processing is limited to the initial 3 to 5 hours, which mainly corresponds to the measurement interval for coated particles (not aged). This implies that a large number of secondary aerosol particles may coagulate with the soot-containing particles. However, the relevance of this process is limited to the pre-ageing measurement period in which the aerosol properties are tracked. This further implies that mass deposition due to coagulation during the ageing is minimal.

For the α-pinene SOA, which is significantly smaller in size and strongly separated in its size distribution from the soot-containing mode, the potential coagulation is significantly less. While a minimal increase in coagulation rate is calculated during the first few minutes of SOA generation, this cannot be considered significant. Further, it has to be noted that the potential for coagulation reduces to a minimum following the SOA generation, contrasting the control and $H_2SO_4$ experiments in which continuous potential coagulation is observed. Fig S10 shows that the potential number and especially mass coagulations are lower than in the reference experiments, and the integrated potential remains rather stable after the initial SOA generation.

Overall, the calculations show that the coating process affects the potential for aerosol coagulation and can be relevant for the processing during the simulation of atmospheric ageing. The relevance of this process, however, differs depending on the secondary aerosol properties and is found to be rather negligible for SOA experiments, contrasting the $H_2SO_4$ experiments, where the contribution has to be considered non-negligible for the coating growth and simulated atmospheric ageing.

**Sect. S3. Calculations of soot SSA from measurements and based on Mie core-shell and fixed $E_{abs}$ approximations**

The single scattering albedo of the BC-containing aerosols ($SSA_{meas}$) was estimated as the ratio of the scattering and extinction coefficients measured during experiments, and subtracting the scattering signal by the SOA and $H_2SO_4$ nucleating modes identified in the size distribution. To this, Mie calculations were performed assuming a refractive index of 1.5-0i for the α-pinene SOA (Denjean et al., 2015; Kim et al., 2010; Schnaiter et al., 2005) and 1.24-0i for $H_2SO_4$ (Heuser et al., 2025).

In the Mie core-shell approximation, the SSA ($SSA_{MieCS}$) was calculated as a function of $M_{R,bulk}$, considering a selected representative soot size distribution, taken from the pre-coating phase. We assume that the volume equivalent size distribution does not change, and only the particle number and coating quantity undergo changes. This choice is supported based on the observation that after the coating formation, only limited coagulation is ongoing, and in particular, only minimal soot-soot-coagulation (identified also in the constant median diameter of the rBC measurement) occurred.
In the approximation of a fixed $E_{abs}$ of 1.5 the SSA ($SSA_{fixed\text{-}1.5}$) was calculated as

$$SSA_{fixed-1.5} = \frac{1}{1 + 1.5\left(\frac{1}{SSA} - 1\right)} . \quad (S8)$$

It should be noted that in the case of fixed $E_{abs}$, due to the lack of information to quantify scattering changes in the two-phase system, only the impact of coating formation on absorption was considered through $E_{abs}$, while scattering was assumed to remain unchanged.

**Table S1.** General concept of the soot ageing experiments, with the specifics of the ageing experiments explained in Text S1.

| STEP | Duration | Time in this steady condition | Action & Objective | Comment |
|---|---|---|---|---|
| *Filling the chamber with $N_2$ and $O_2$* | 15 min | 1 hour | Connecting instruments to verify the background | |
| *Soot injection + characterisation of fresh soot* | 0.5 to 7 min | ~ 2 hours | Measurement of the aerosol physico-chemical and spectral optical properties, gas phase, and chamber thermodynamic state to determine initial conditions | For soot injection, specific instruments were disconnected (TEOM, optics, gas monitors) to adjust compensation and avoid measurement instabilities by pressure changes; reconnected a few minutes later. |
| *Soot ageing including multiple steps* | ~ 2 hours | 2 to 23 hours | Measurement of the aerosol physico-chemical and spectral optical properties, gas phase, and chamber thermodynamic state to determine evolution compared to initial conditions | |
| *Instruments disconnection and pumping* | 30 min | NA | End of experiment, chamber evacuation until the next experiment | |

**Table S2.** List of full instrumentation used to determine the properties of the aerosol particulate phase during the soot experiments in CESAM, as fully described in Heuser et al. (2025). Instrument model, measured or derived parameters, time resolution, uncertainty, and main reference or specific data treatment for each technique are provided. For all optical instruments, measurements on HEPA-filter and on the aerosol-free chamber were used to determine their current instrumental background noise level, then used to determine the noise-signal-ratio. The instruments and measurements used in the present analysis are described in the main manuscript.

| Instrument | Measured or derived parameter (units) | Time resolution | Associated Uncertainties | | Reference |
|---|---|---|---|---|---|
| **SMPS System TSI (DMA 3080 & CPC 3772; 2.0/0.2 L $min^{-1}$ sheath/aerosol flow rates)** | number size distribution [# $cm^{-3}$] in the 19.5 to 881.7 nm mobility diameter range | 180 s | 3% + counting error | Error propagation considering 3% DMA uncertainty in particle mobility size selection, plus counting error as the standard deviation of an assumed Poisson distribution | (DeCarlo et al., 2004) |
| **TSI DMA 3080 + CPMA (Cambustion) + CPC 3775 high** | $\rho_{eff}$ (effective density) [g $cm^{-3}$] from the mass-resolved number size distribution [# $cm^{-3}$] | 30-45 min, with 180 s at each selected mass | 10% | Error propagation considering DMA uncertainty, mass-to-charge uncertainty, and relative standard error of the size distribution median diameter For mass calculation, the uncertainty in the power law fit under consideration of the eff. density uncertainties is used | (Olfert and Collings, 2005) (Yon et al., 2015) |
| **TEOM 1400a Thermo Scientific** | mass concentration [µg $m^{-3}$] | 300 s | 15% | Determined from noise operating on the chamber (determined on clean chamber values and following smoothed variability) | |
| **CPC 3775 TSI** | particle number (> 4 nm) [# $cm^{-3}$] | 1 s | 10% | | |
| **SP2 Droplet Measurement Technologies (DMT)** | Refractory BC (rBC) mass concentration [µg $m^{-3}$] rBC number size distribution [# $cm^{-3}$] | 60 s | 17% | Following (Laborde et al., 2012) | (Stephens et al., 2003) |
| **Integrating Nephelometer 3563 TSI** | scattering coefficient [$Mm^{-1}$] at 450, 550 and 700 nm | 1 s | 8% | Propagation of uncertainties from cross-calibration (against freshly calibrated Nephelometer), truncation correction, and signal-to-noise ratio (averaged for different total loss conditions) | (Anderson et al., 1996) (Massoli et al., 2009) |
| **CAPS $PM_{ex}$ Aerodyne** | extinction coefficient [$Mm^{-1}$] at 450 and 630 nm | 1 s | 5-6% | Propagation of uncertainties for general measurement precision (3%;(21)) and signal-to-noise ratio (averaged for different total loss conditions) | (Kebabian et al., 2007) (Massoli et al., 2010) |
| **CAPS $PM_{SSA}$ Aerodyne** | extinction coefficient [$Mm^{-1}$] 450 and 630 nm (only extinction signal used) | 1 s | 5-6% | Propagation of uncertainties for general measurement precision and signal-to-noise ratio (see above) | (Onasch et al., 2015) |
| **CAPS $PM_{ex}$ Aerodyne/ Integrating Nephelometer 3563 TSI** | absorption coefficient [$Mm^{-1}$] 450 and 630 nm (extinction minus scattering) | 1 s | 10-30% | Propagation of uncertainties from the measurements of scattering and absorption, including the uncertainties from the interpolation of the scattering signal to 630 nm | |
| **MAAP Thermo-Scientific** | absorption coefficient [$Mm^{-1}$] 637 nm wavelength | 60 s | 12% | Provided in the instrument's literature | (Petzold et al., 2005; Petzold and Schönlinner, 2004) |
| **MWAA (Multi-Wavelength Absorbance Analyser)** | absorption coefficient [$Mm^{-1}$] 375, 405, 532,635, 850 nm | 15-120 min | mean - 19% | Provided by Massabò and team (var. based on filter loading) | (Massabò et al., 2013) |
| **PP_UniMI (Polar photometer)** | absorption coefficient [$Mm^{-1}$] 405, 448, 532, 635, 780 nm | 15-120 min | mean - 14% | Provided by Vecchi and team (var. based on filter loading) | (Vecchi et al., 2014) |
| **TEM JEOL® 100CXII microscope and a JEOL JEM2010** | Particle imaging and morphology characterization | 30 sec to 120 min | - | $D_{pp}$, $D_f$, and $k_f$ as output from Bescond (Bescond et al., 2014) average used is determined using a single determination of all CS1 pictures | |

**Table S3.** List of instrumentation used to characterize the gas phase and the thermodynamic state of the chamber during the soot experiments in CESAM. Instrument model, measured parameters, time resolution, accuracy, and detection limit of data are provided.

| Instrument | Parameter (units) | Acquisition resolution | Accuracy (at 1 min time resolution) & detection limit (Acc./DL) |
|---|---|---|---|
| **$NO_x$ Monitor – Horiba APNA370** | NO, $NO_2$ (NOx) [ppb] | 5 s | 1 / 0.5 ppb |
| **APEE - ProCeas** | CO/$CO_2$ [ppm] | 45 s | 0.1/ 0.05 ppm |
| **$SO_2$ Monitor - Horiba APSA370** | $SO_2$ [ppb] | 5 s | 1/ 0.05 ppb |
| **Ozone ($O_3$) Monitor - Horiba APOA370** | $O_3$ [ppb] | 5 s | 1 / 0.05 ppb |
| **Teledyne T500U** | $NO_2$ [ppb] | 30 s | 0.5% (above 5 ppb)/ 0.04 ppb |
| **Hygrometer - Vaisala HMP234** | RH [%] & T [°C] | 1 s | 2% & ± 0.1 °C (only Acc.) |
| **Baratron type MKS 626AX13TDE (high)/ 626AX11TDE (low)** | Pressure [mBar] | 1 s | 0.25% for 1 to 1000 Torr (Unc.) |
| **PTR-ToF-MS (Kore ltd.)** | Mass-loading gaseous components [ppb] | 60 s | 0.1 ppb [DL] |

**Figure S1** Probability distribution of the averaged mass absorption cross sections (MAC) at 450 and 630 nm for the studied control experiments. The dashed curve and the grey area represent the average and one standard deviation of the probability distribution of the MAC for fresh soot measurements (5.9 ± 0.9 $m^2$ $g^{-1}$ at 450 nm, and 4.3 ± 0.7 $m^2$ $g^{-1}$ at 630 nm) as reported in Heuser et al. (2025).

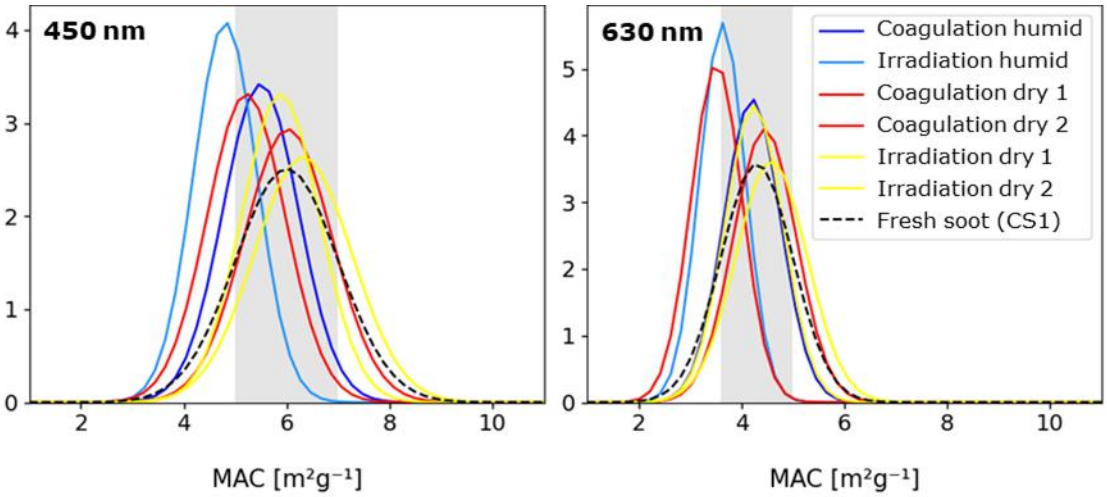


**Figure S2** Timeline for the $H_2SO_4$ coating experiments showing the evolution of a) the count median diameter (CMD) of the soot peak mode, b) the bulk coating-to-soot mass ratio ($M_{R,bulk}$), c) the enhancement factor of the absorption ($E_{abs}$) at 450 nm, and d) 630 nm.

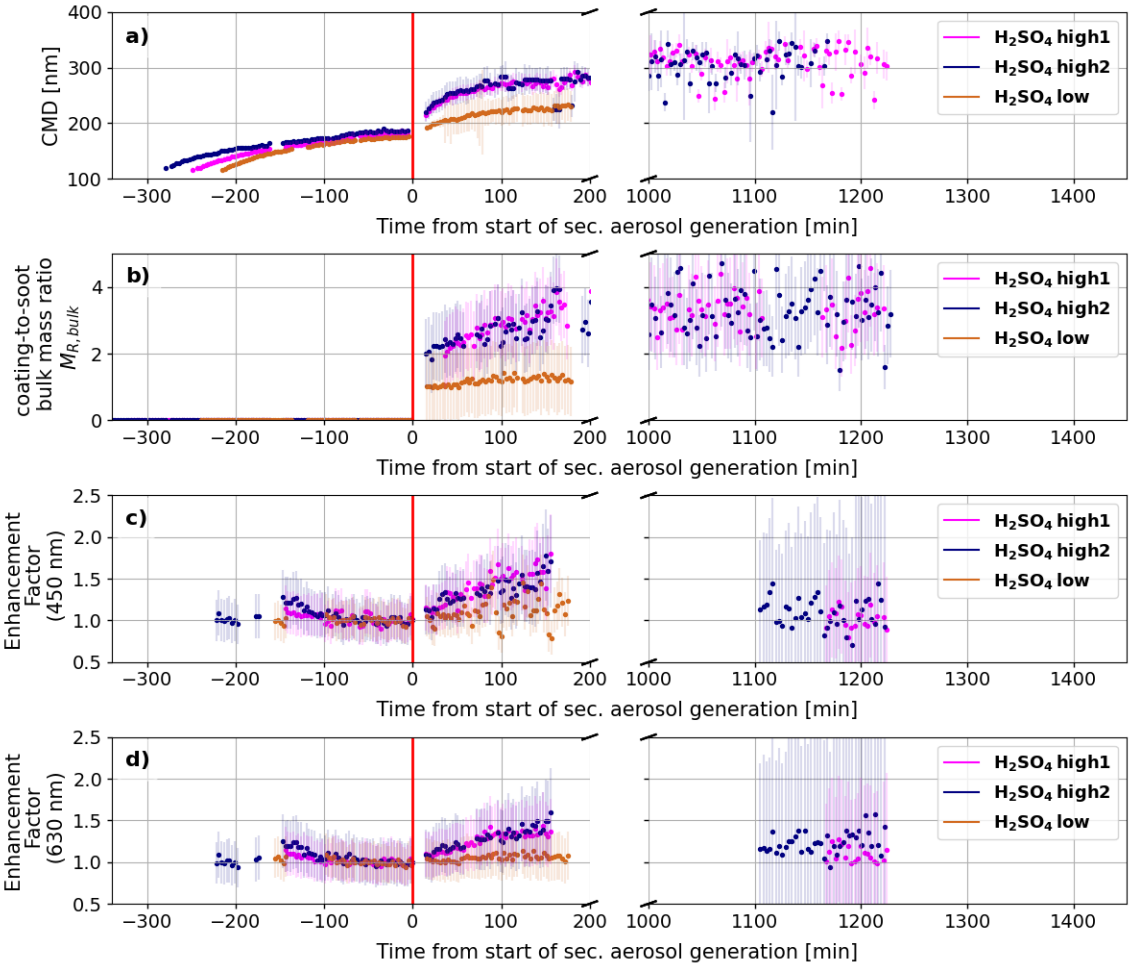


**Figure S3** Timeline for the α-pinene-SOA coating experiments showing the evolution of a) the count median diameter (CMD) of the soot peak mode, b) the bulk coating-to-soot mass ratio ($M_{R,bulk}$), c) the enhancement factor of the absorption ($E_{abs}$) at 450 nm, and d) 630 nm.

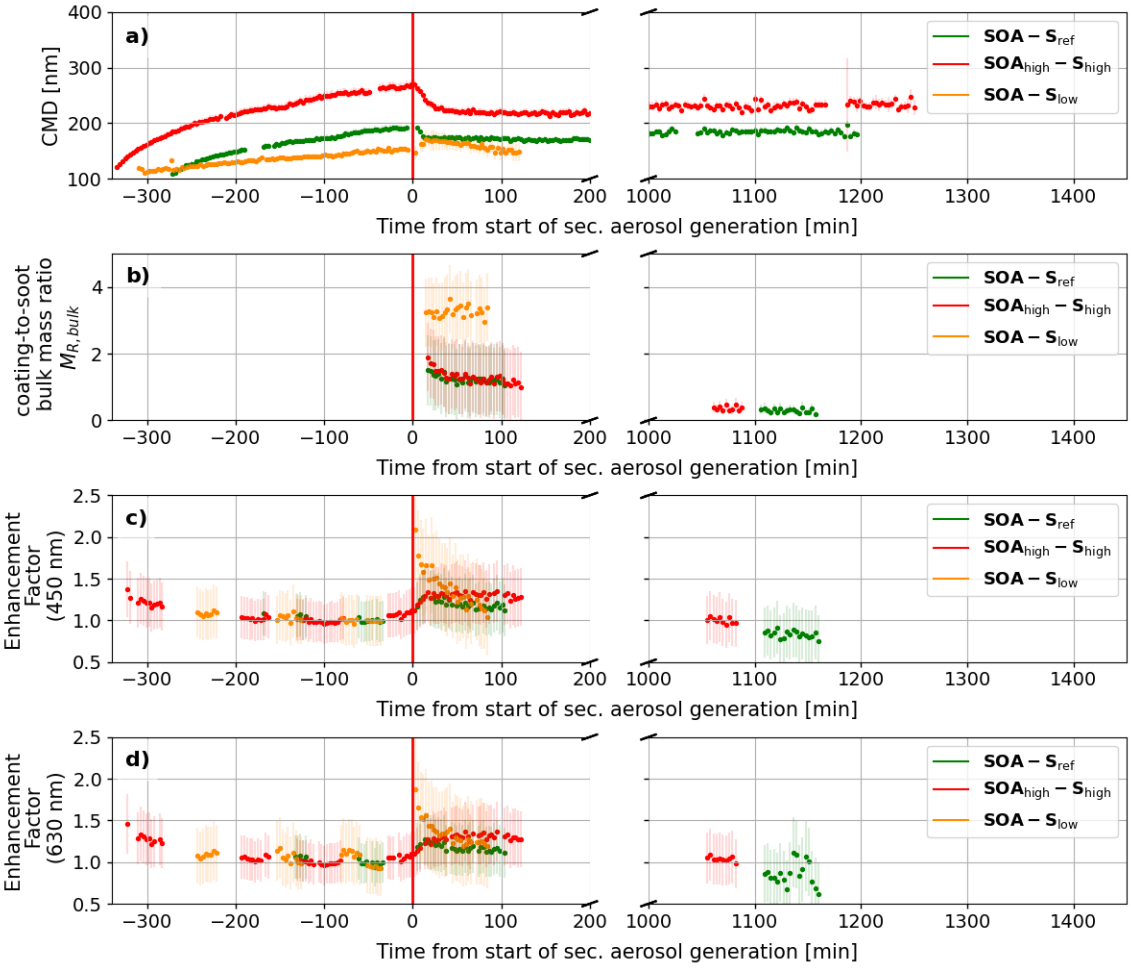


**Figure S4.** Overview of selected TEM images of soot containing particles from the 3 stages of the $H_2SO_4$ coating experiments: *Fresh* (reference point for pre-coating condition; sampled about 15 to 90 min after soot injection), *Coated* (sampled about 15 to 120 minutes after start of the coating production), and *Aged* (sampled 60 to 240 minutes after the long-ageing of the coated soot). Pictures are selected in order to present an overall impression of the soot structures observed.

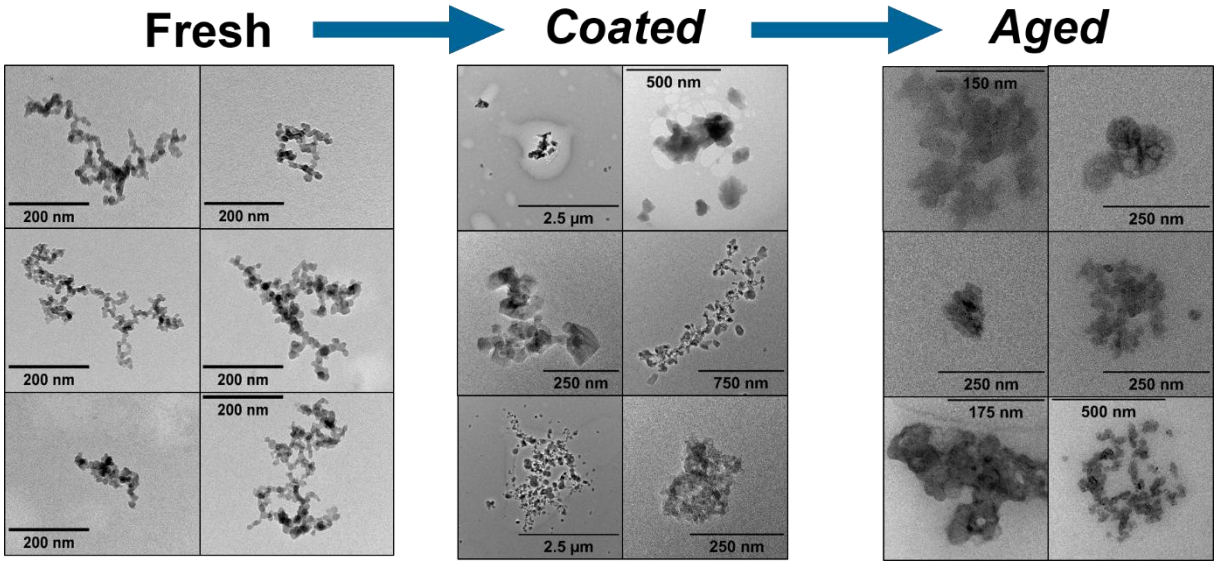



**Figure S5.** Overview of selected TEM images of soot containing particles from the 3 stages of the SOA coating experiments: *Fresh* (reference point for pre-coating condition; sampled about 15 to 90 min after soot injection), *Coated* (sampled about 15 to 120 minutes after start of the coating production), and *Aged* (sampled 60 to 240 minutes after the long-ageing of the coated soot). Pictures are selected in order to present an overall impression of the soot structures observed.

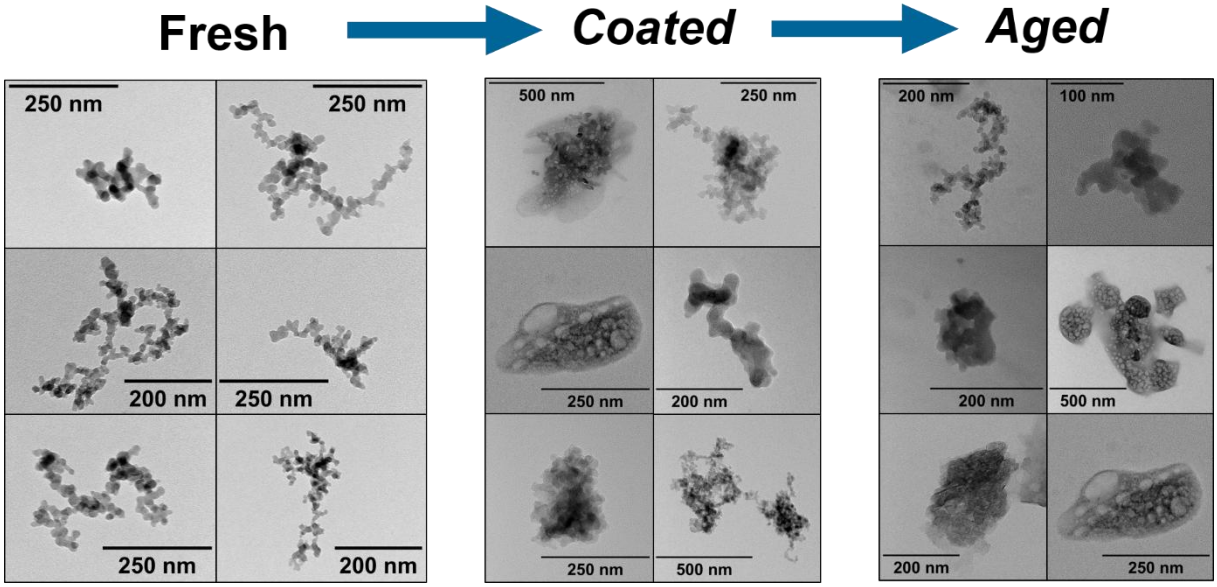


**Figure S6** Absorption enhancement factor ($E_{abs}$) at 450 nm as a function of the coating-to-soot mass ratio ($M_{R,bulk}$) for (A) the $H_2SO_4$ and (B) the α-pinene SOA coating experiments with their uncertainty on both variables. Symbols and color separate the measured data of different experiments. Slightly transparent values are measured during the initial 60 and points with black edges are taken after the ageing. Groupings of pre- (green) and post-ageing (red) values are manually highlighted using coloured ellipses. Additionally, the theoretical calculations using the Mie core-shell approximation for the different coating types are shown. The $E_{abs}$ core-shell curves are reported for the value of the real part corresponding to the refractive index associated with the coating material: a value of $n_{shell}$=1.5 for the SOA and $n_{shell}$=1.24 for $H_2SO_4$. The refractive index of the soot core ($n_{core}$) is set at a) 1.95 – 0.79i, representative of BC based on Bond and Bergstrom (2006), and at b) 1.46-0.3i (Habib and Vervisch, 1988) as it represents a value on the other end of the refractive index range associated with soot.

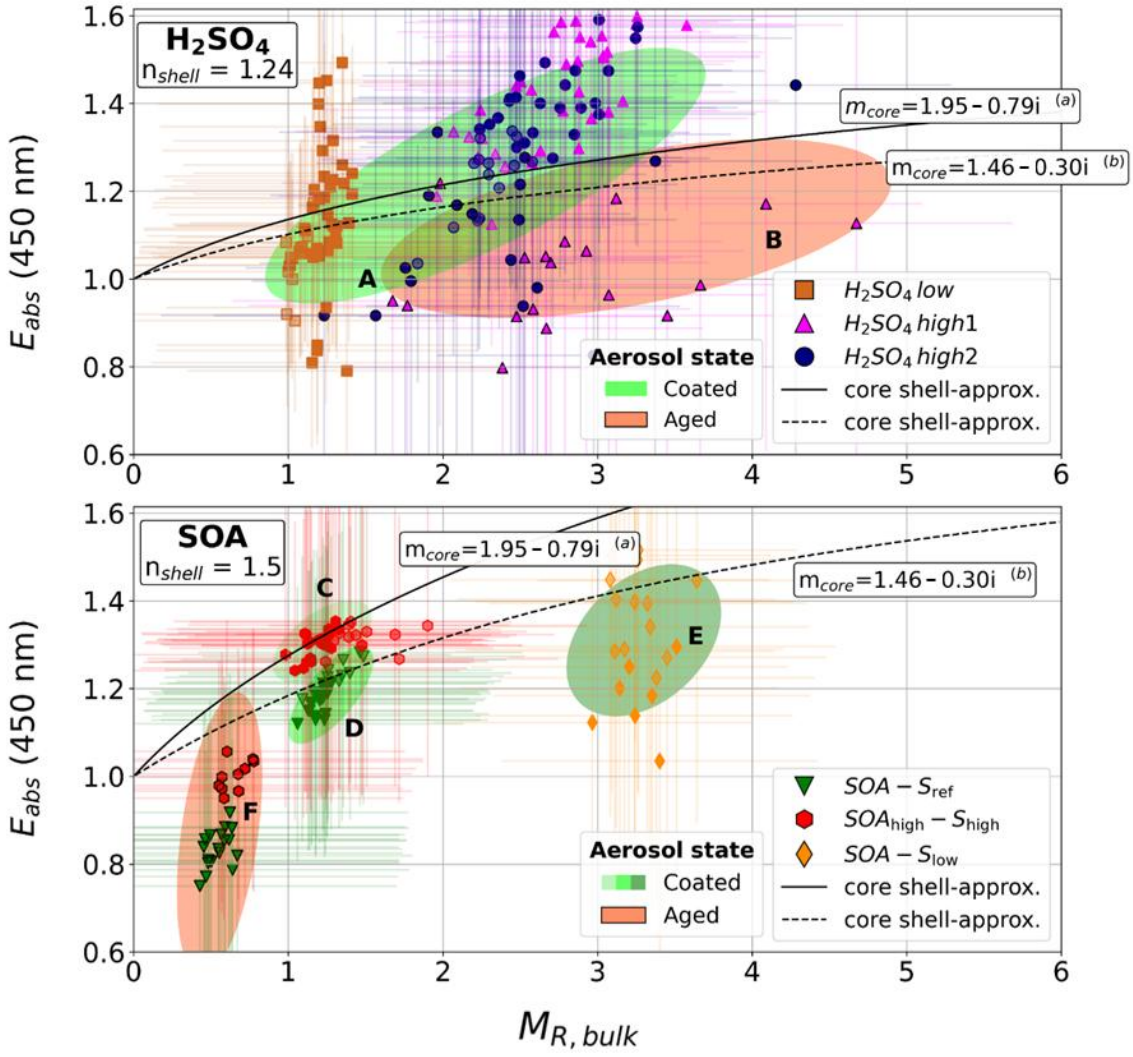


**Figure S7** Absorption enhancement factor ($E_{abs}$) at 630 nm as a function of the coating-to-soot mass ratio ($M_{R,bulk}$) for (A) the $H_2SO_4$ and (B) the α-pinene SOA coating experiments with their uncertainty on both variables. Symbols and color separate the measured data of different experiments. Slightly transparent values are measured during the initial 60 and points with black edges are taken after the ageing. Groupings of pre- (green) and post-ageing (red) values are manually highlighted using coloured ellipses. Additionally, the theoretical calculations using the Mie core-shell approximation for the different coating types are shown. The $E_{abs}$ core-shell curves are reported for the value of the real part corresponding to the refractive index associated with the coating material: a value of $n_{shell}$=1.5 for the SOA and $n_{shell}$=1.24 for $H_2SO_4$. The refractive index of the soot core ($n_{core}$) is set at a) 1.95 – 0.79i, representative of BC based on Bond and Bergstrom (2006), and at b) 1.46-0.3i (Habib and Vervisch, 1988) as it represents a value on the other end of the refractive index range associated with soot.

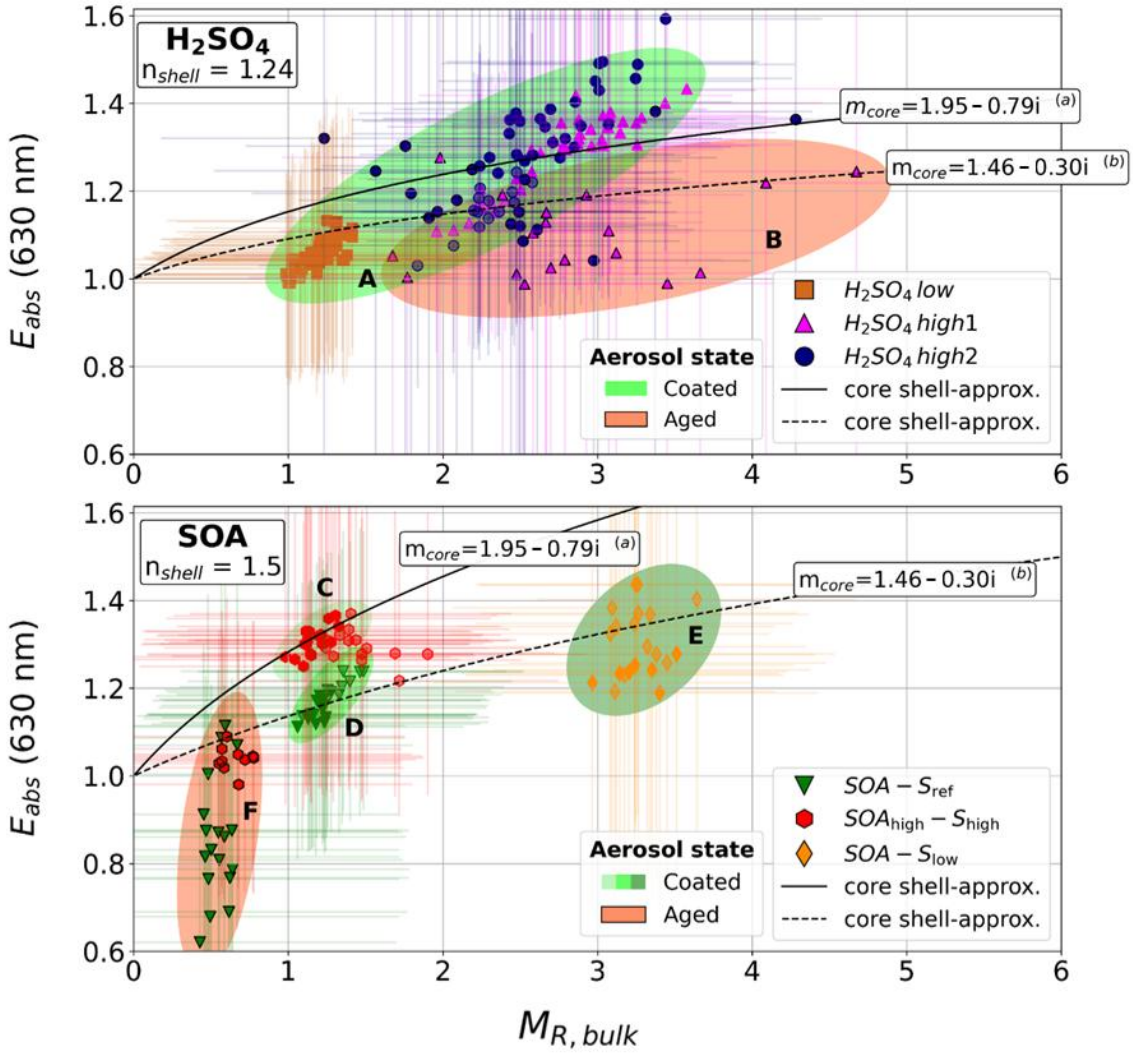


**Figure S8** Effective density measured as a function of the mobility diameter, $\rho_{eff}(D_m)$, for the $H_2SO_4$ (top) and α-pinene SOA (bottom) coating experiments. The power-law fits of $\rho_{eff}(D_m)$ based on Eq. 1 in the main manuscript (coloured lines) and the fitting uncertainties (coloured-shaded areas) are shown. As a reference, the measurements of each ageing step of $H_2SO_4$-high1 (a) and SOA-$S_{ref}$ (b) are shown with their power-law fits as both a reference for fresh soot and the time-dependent evolution of the soot properties.

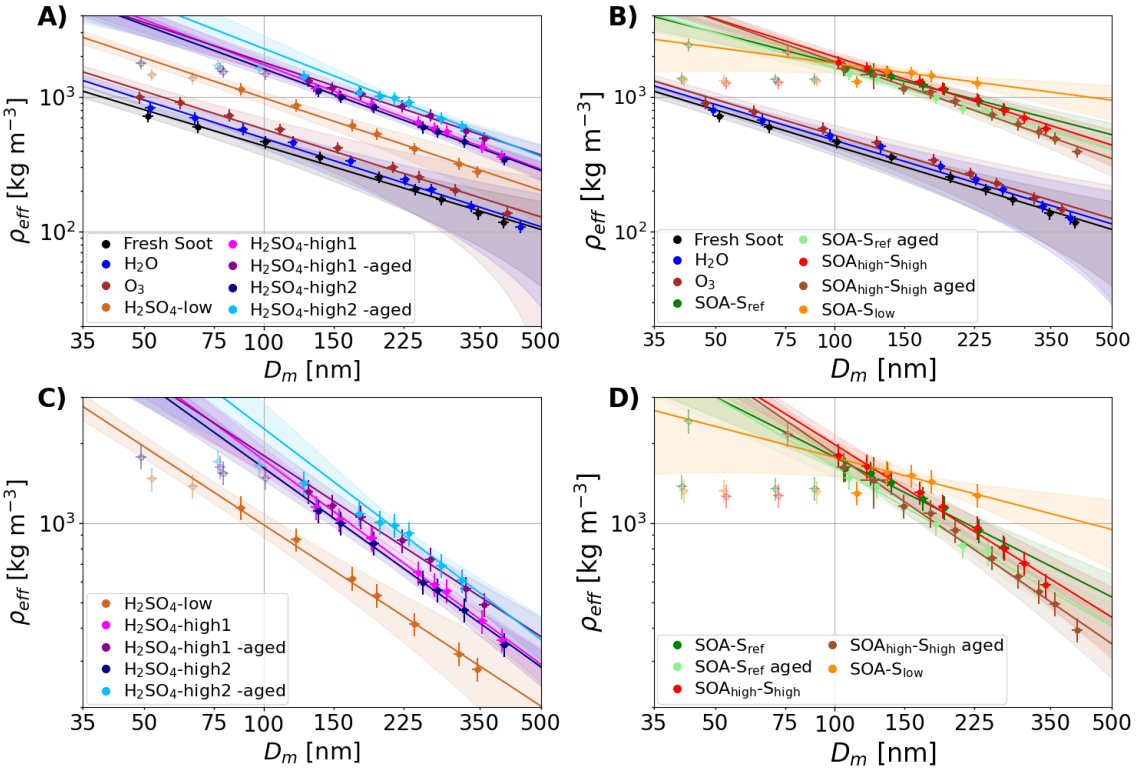


**Figure S9** Overview of the coagulation during the $H_2SO_4$-coating experiments. The upper plot shows the number of potential coagulation of particles with soot particles normalized with the initial particle concentration as discussed in Text S2. The lower plot displays the potential mass that could coagulate onto the soot, normalized by the initial mass concentration of soot particles inside the chamber. Vertical lines mark the start of the secondary aerosol generation in the different experiments. Additionally, to the coating experiments, these values are also given for CS1 coagulation dry 1 ($Soot_{ref}$; black) and CS1 coagulation dry 2 ($Soot_{high}$; grey) as a comparison for soot coagulation without secondary aerosol generation.

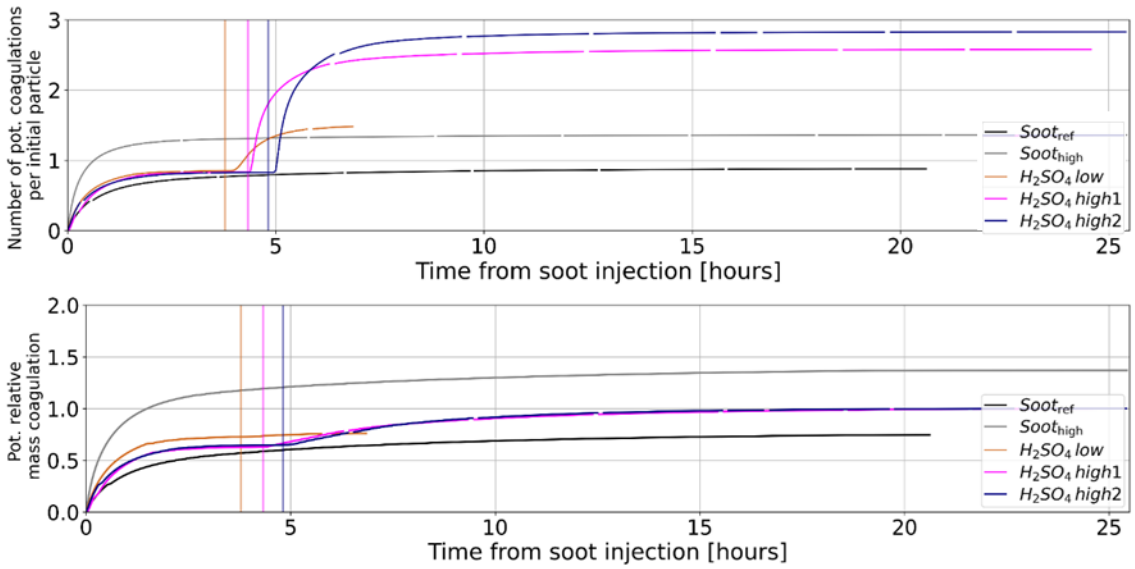


**Figure S10** Overview of the coagulation during the SOA-coating experiments. The upper plot shows the number of potential coagulation of particles with soot particles normalized with the initial particle concentration as discussed in Text S2. The lower plot displays the potential mass that could coagulate onto the soot, normalized by the initial mass concentration of soot particles inside the chamber. Vertical lines mark the start of the secondary aerosol generation in the different experiments. Additionally, to the coating experiments, these values are also given for CS1 coagulation dry 1 ($Soot_{ref}$; black) and CS1 coagulation dry 2 ($Soot_{high}$; grey) as a comparison for soot coagulation without secondary aerosol generation.

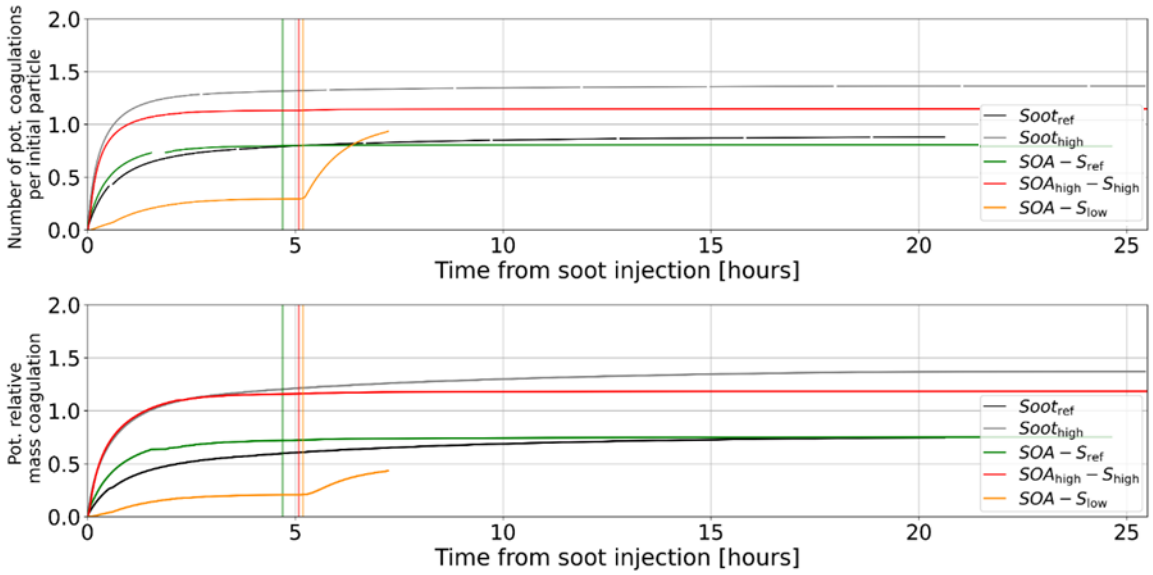


**Figure S11** Multi-panel figure of the $H_2SO_4$-low experiment. From top to bottom: the upper panel shows the aerosol number size distribution from the SMPS, with the fitted CMD for all modes (black=soot, other colors=secondary aerosol). Vertical lines indicate the occurrence of various events during the experiment (injection of soot, water vapor, $O_3$, $SO_2$, start and stop of irradiation (lamp and lamp off). The second panel shows the refractory black carbon number distribution and its fitted median diameter. The third panel shows the mass concentration of the aerosol with $m_{total}$ determined from the SMPS and different effective densities for each event (different colors), the mass of the nucleated secondary aerosol ($m_{free}$, indicated as $m_{nuc}$ in the main manuscript), and the $m_{soot}$ from the SP2. Panel four displays the mass absorption cross section (MAC) at 450 and 630 nm calculated with both $m_{soot}$ and $m_{total}$. The absorption enhancement factor ($E_{abs}$) is shown in the fifth panel. Panel six shows the gas concentration of a selection of gases. The bottom panel shows the effective density measurements done during this experiment.

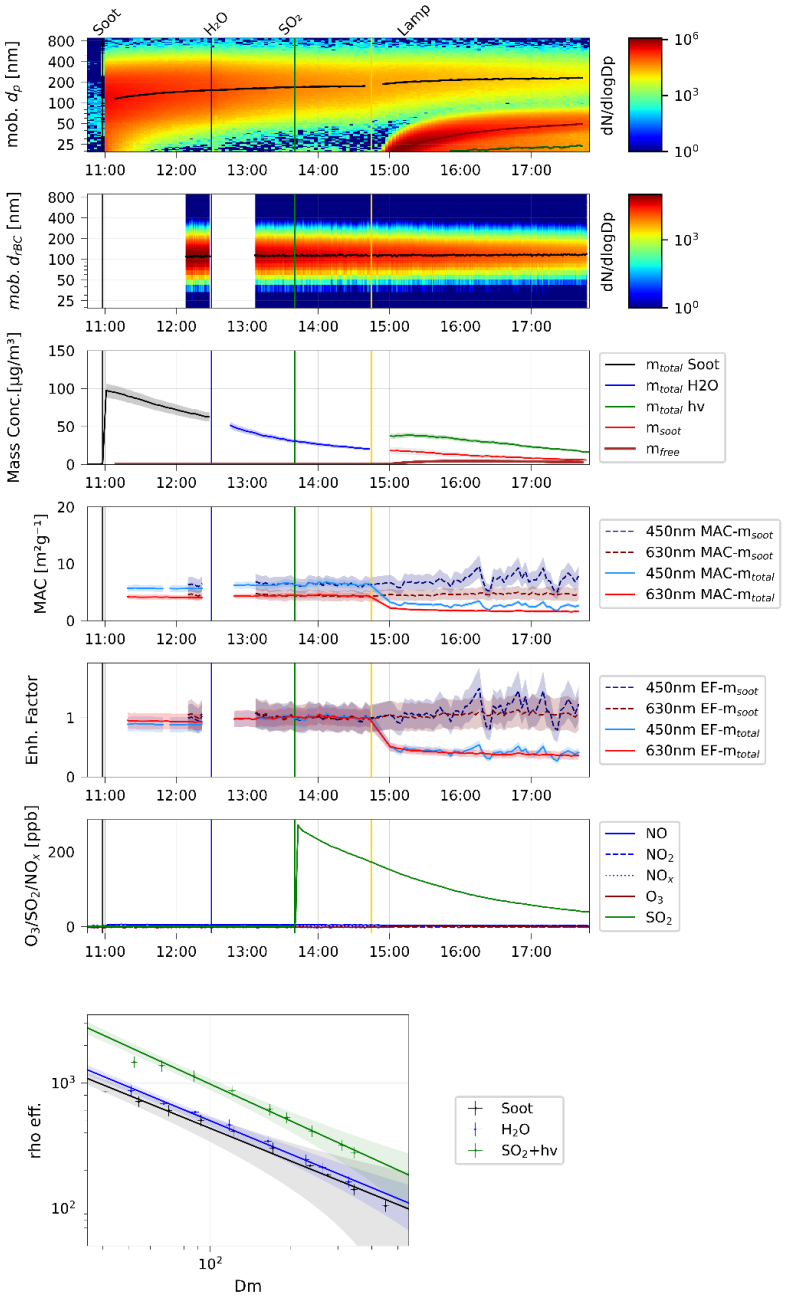


**Figure S12** Same as Fig. S11 for the $H_2SO_4$-high1 experiment.

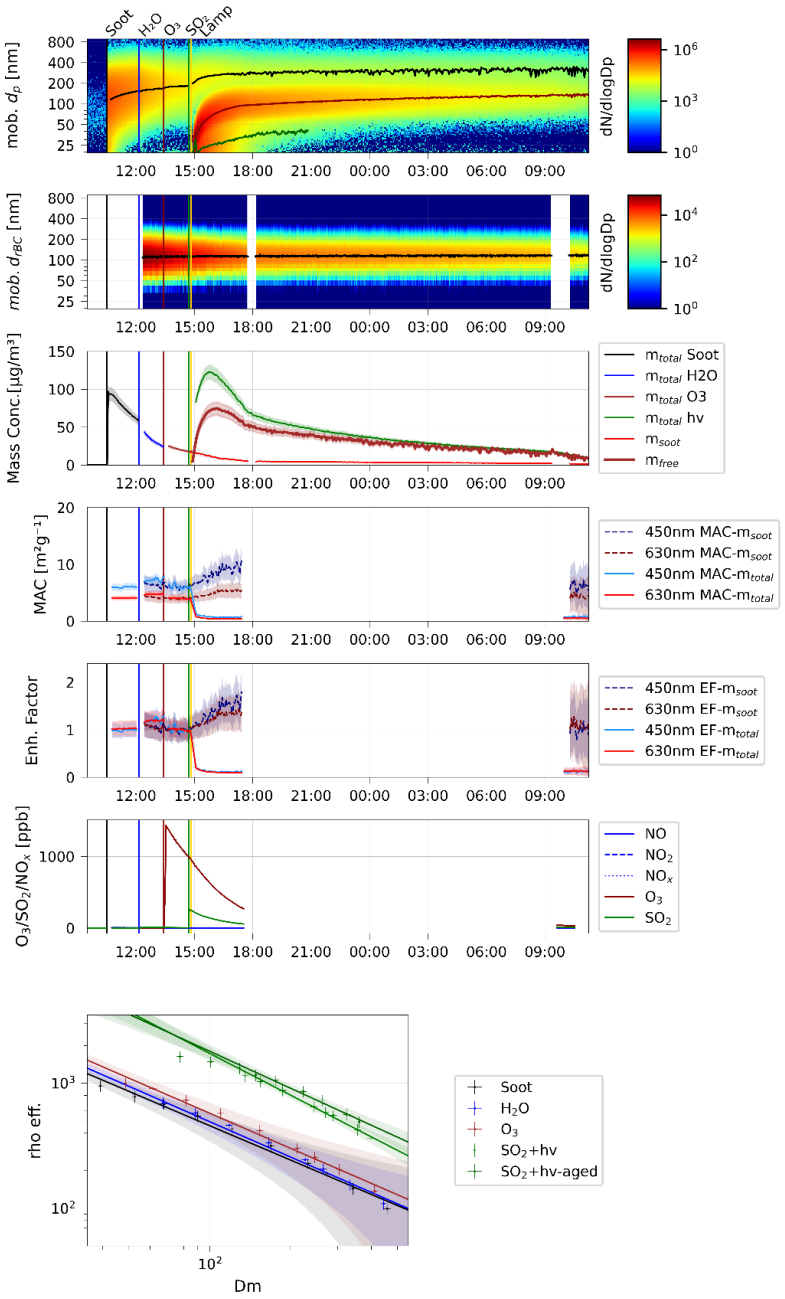


**Figure S13** Same as Fig. S11 for the H2SO4-high2 experiment.

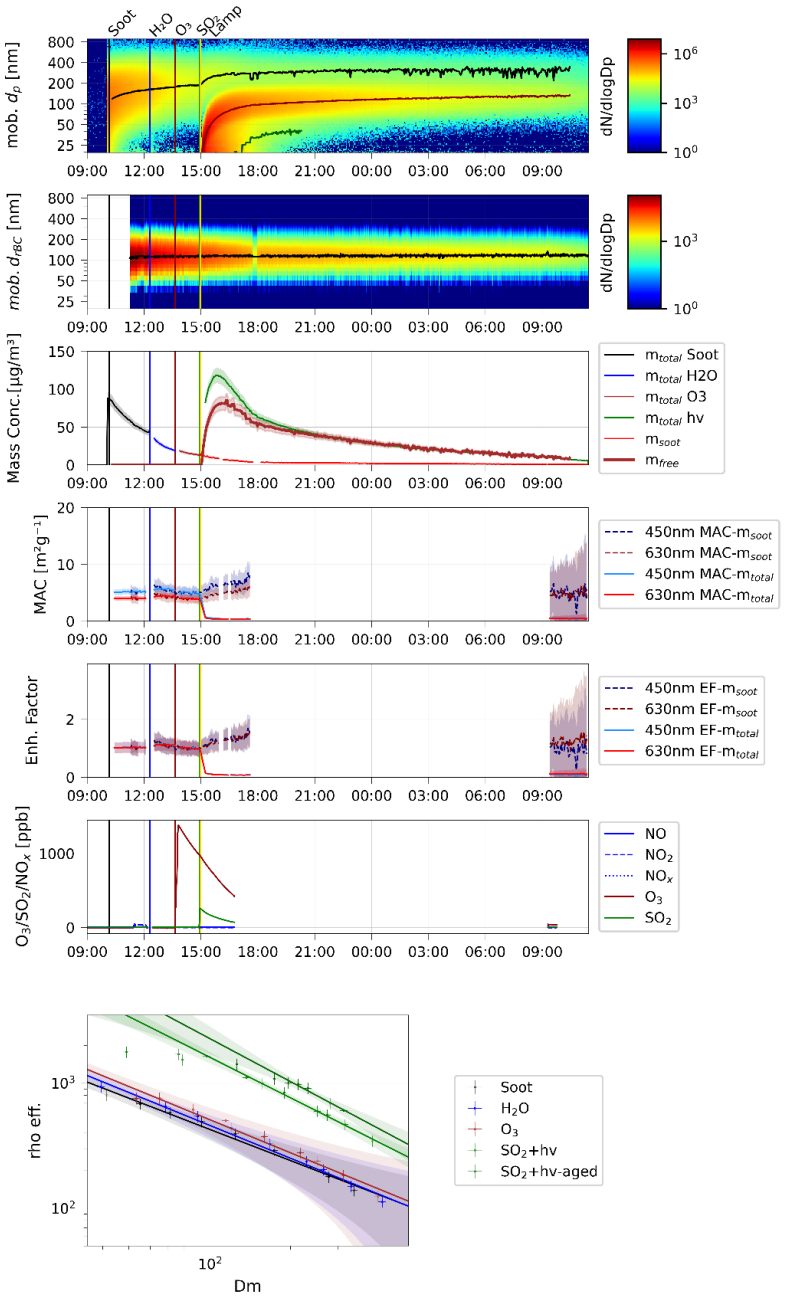


**Figure S14** Same as Fig. S11 for the SOA-$S_{Ref}$ experiment.

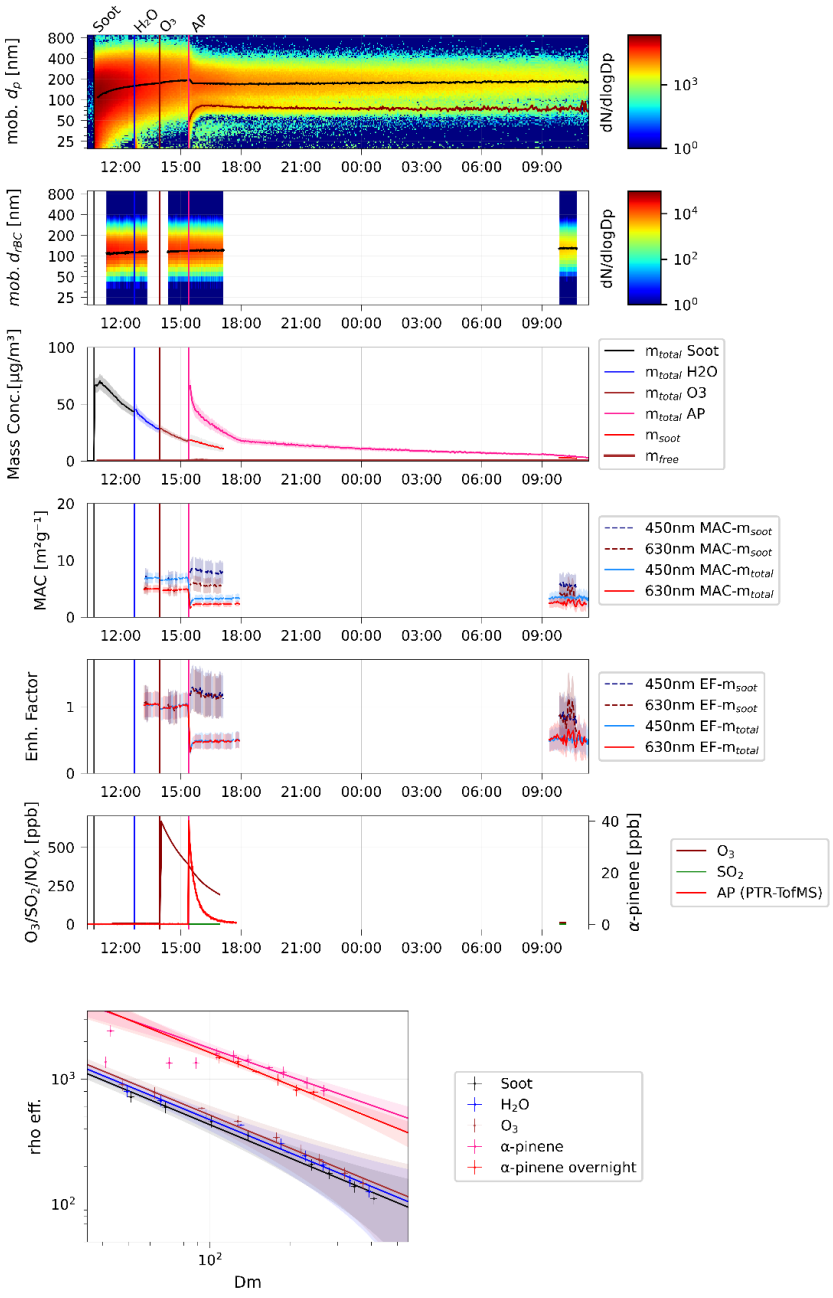


**Figure S15** Same as Fig. S11 for the $SOA_{high}$-$S_{high}$ experiment.

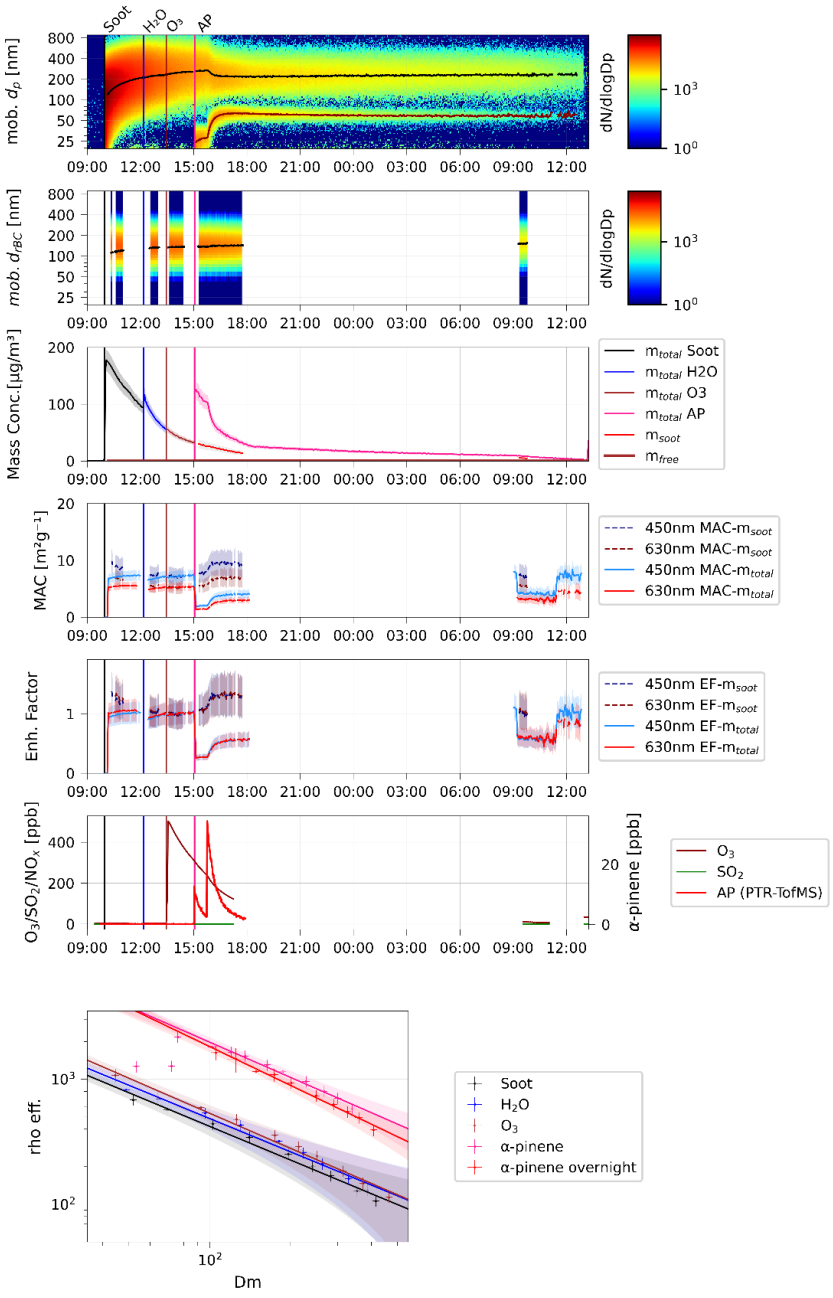


**Figure S16** Same as Fig. S11 for the SOA-$S_{low}$ experiment.

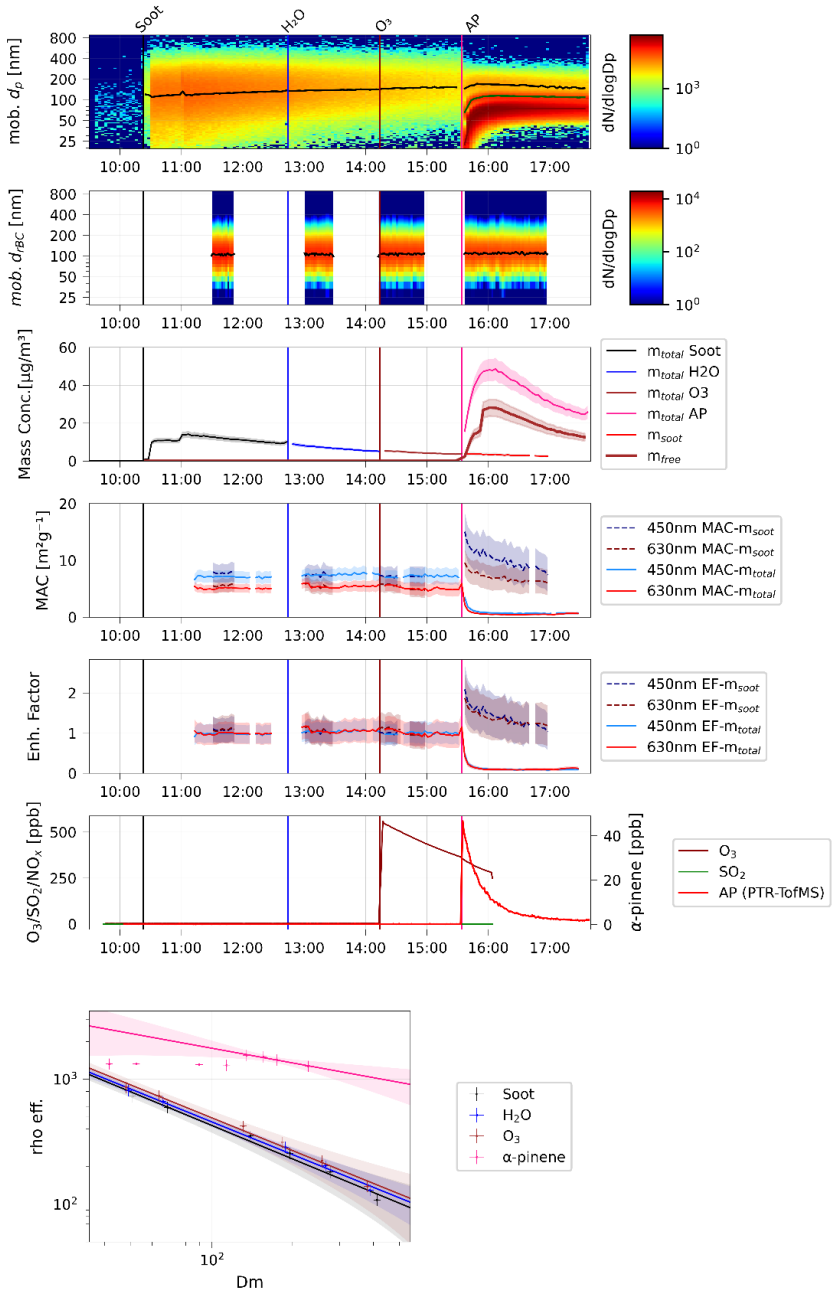


**Figure S17** Same as Fig. S11 for the CS1 coagulation dry1 experiment. To note that, differently from Fig. S11-S16, the MAC and EF values are calculated here using $m_{total}$.

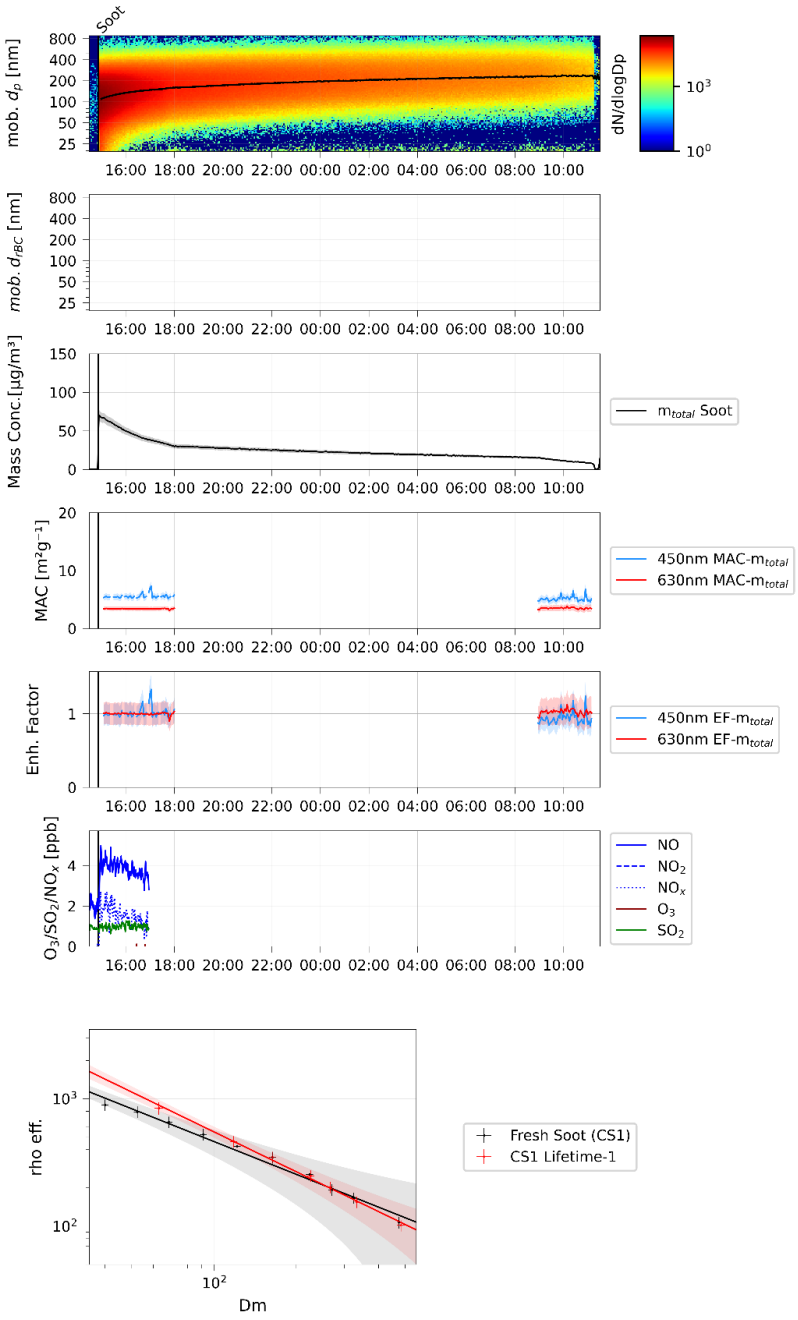


**Figure S18** Same as Fig. S11 for the CS1 coagulation dry2 experiment. To note that, differently from Fig. S11-S16, the MAC and EF values are calculated here using $m_{total}$.

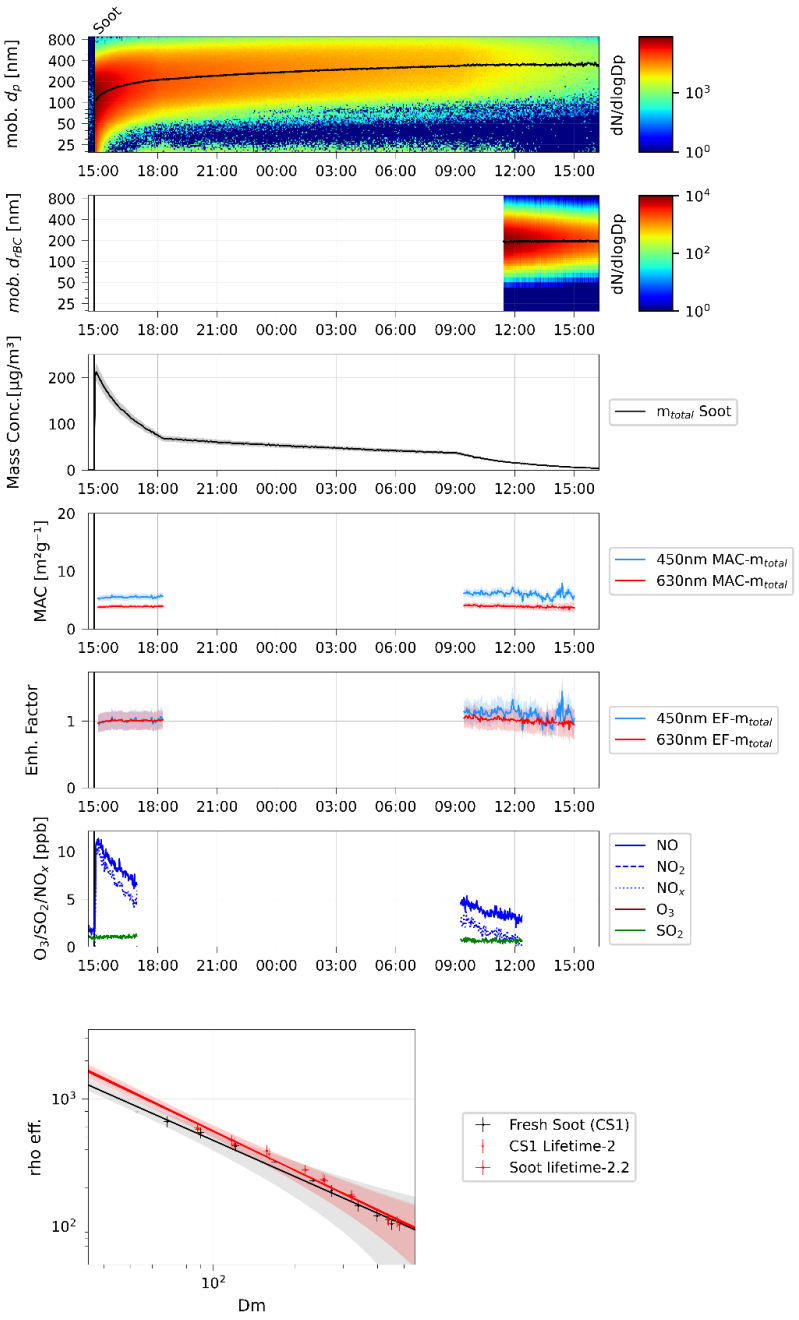


**Figure S19** Same as Fig. S11 for the CS1 irradiation dry 1 experiment. To note that, differently from Fig. S11-S16, the MAC and EF values are calculated here using $m_{total}$.

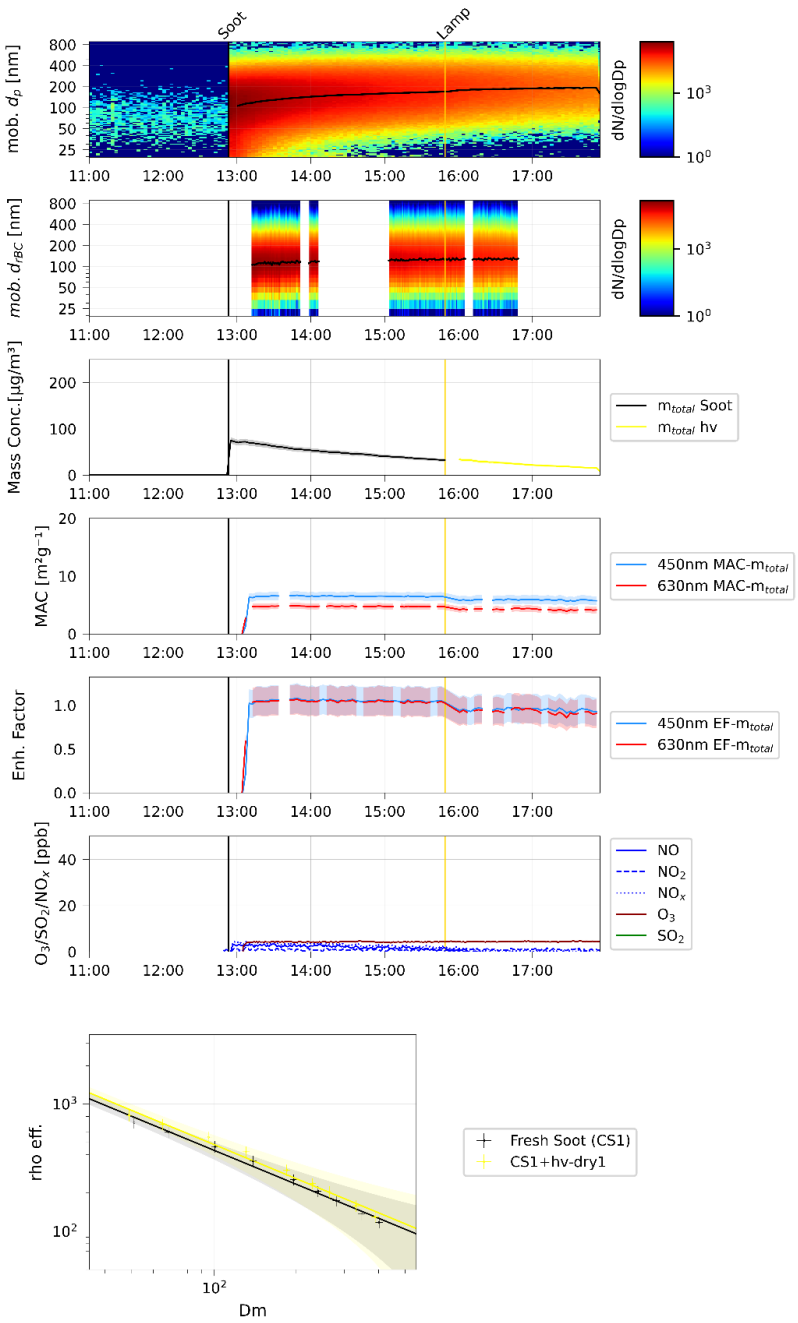


**Figure S20** Same as Fig. S11 for the CS1 irradiation dry 2 experiment. To note that, differently from Fig. S11-S16, the MAC and EF values are calculated here using $m_{total}$.

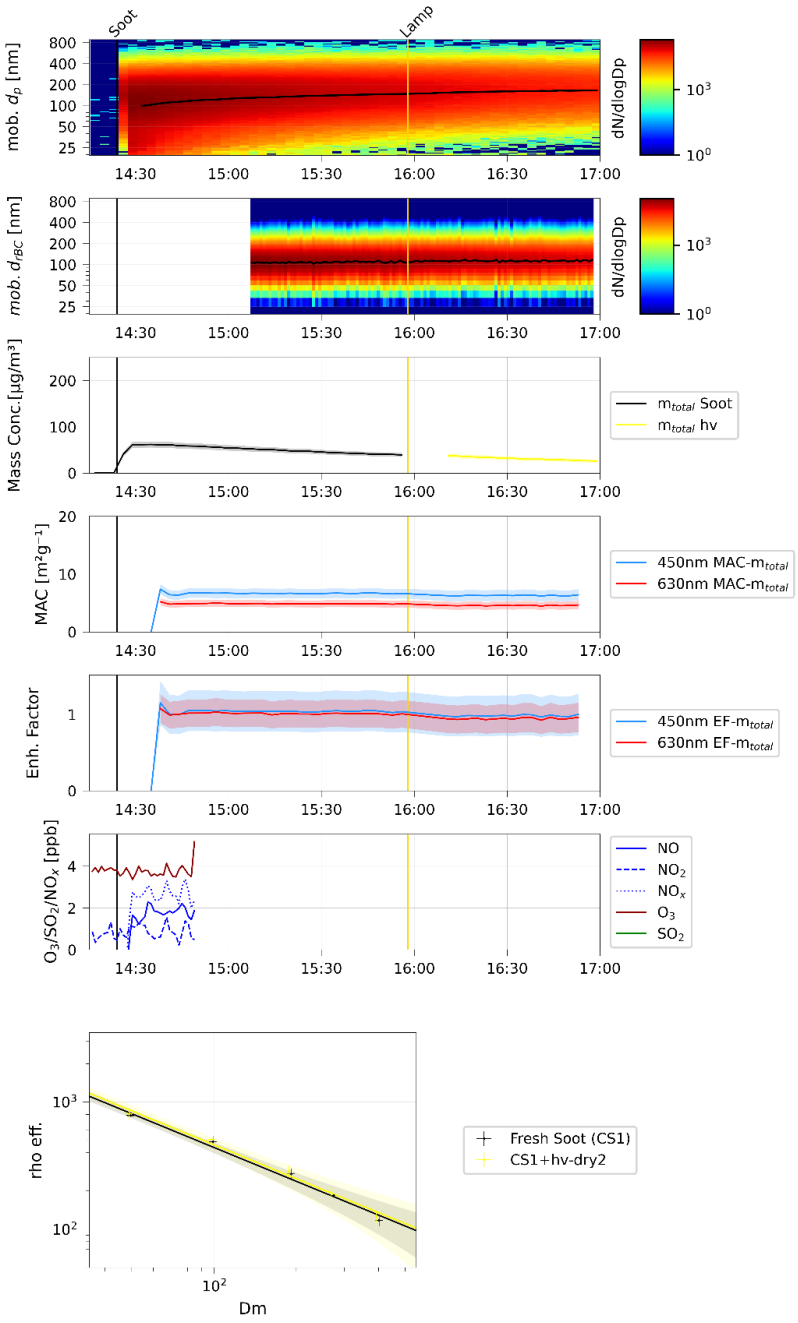


**Figure S21** Same as Fig. S11 for the CS1 coagulation humid experiment. To note that, differently from Fig. S11-S16, the MAC and EF values are calculated here using $m_{total}$.

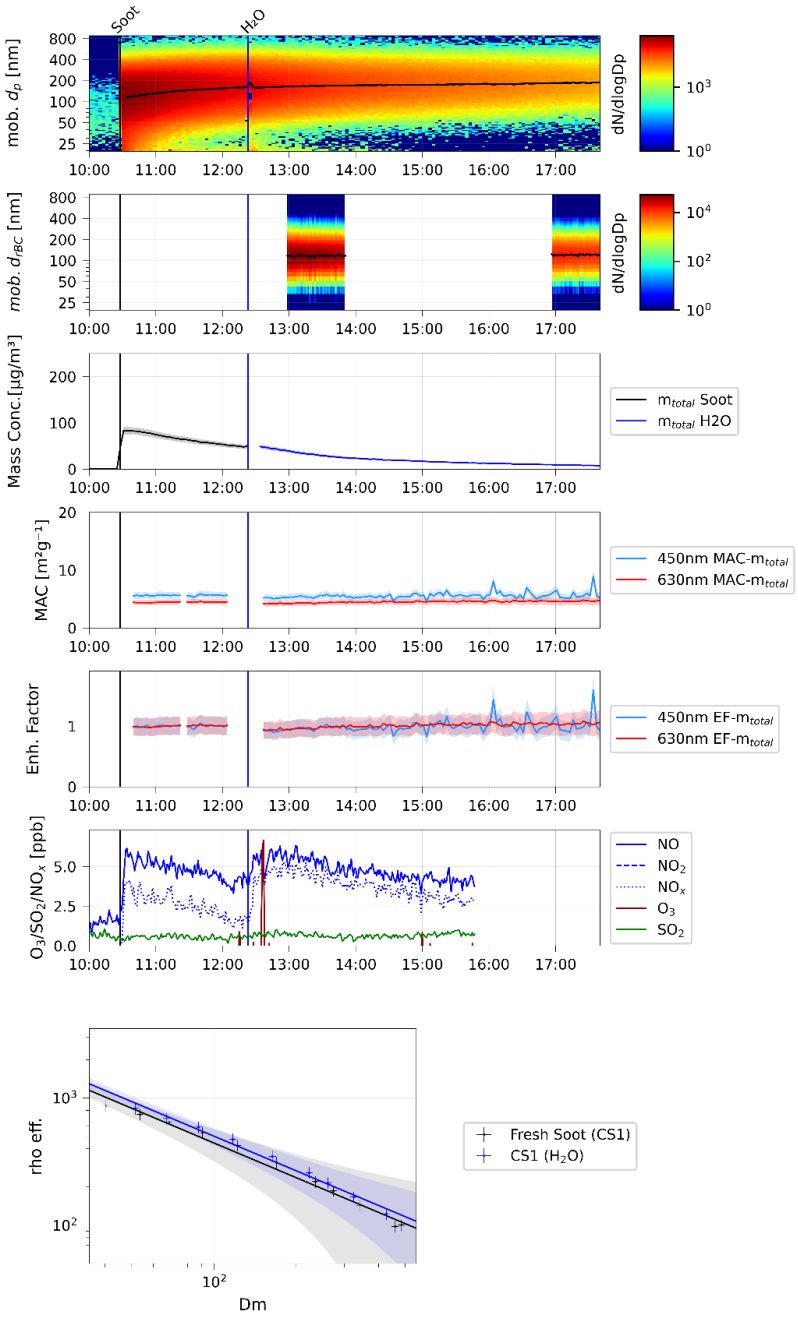


**Figure S22** Same as Fig. S11 for the CS1 irradiation humid experiment. To note that, differently from Fig. S11-S16, the MAC and EF values are here only calculated using $m_{total}$.

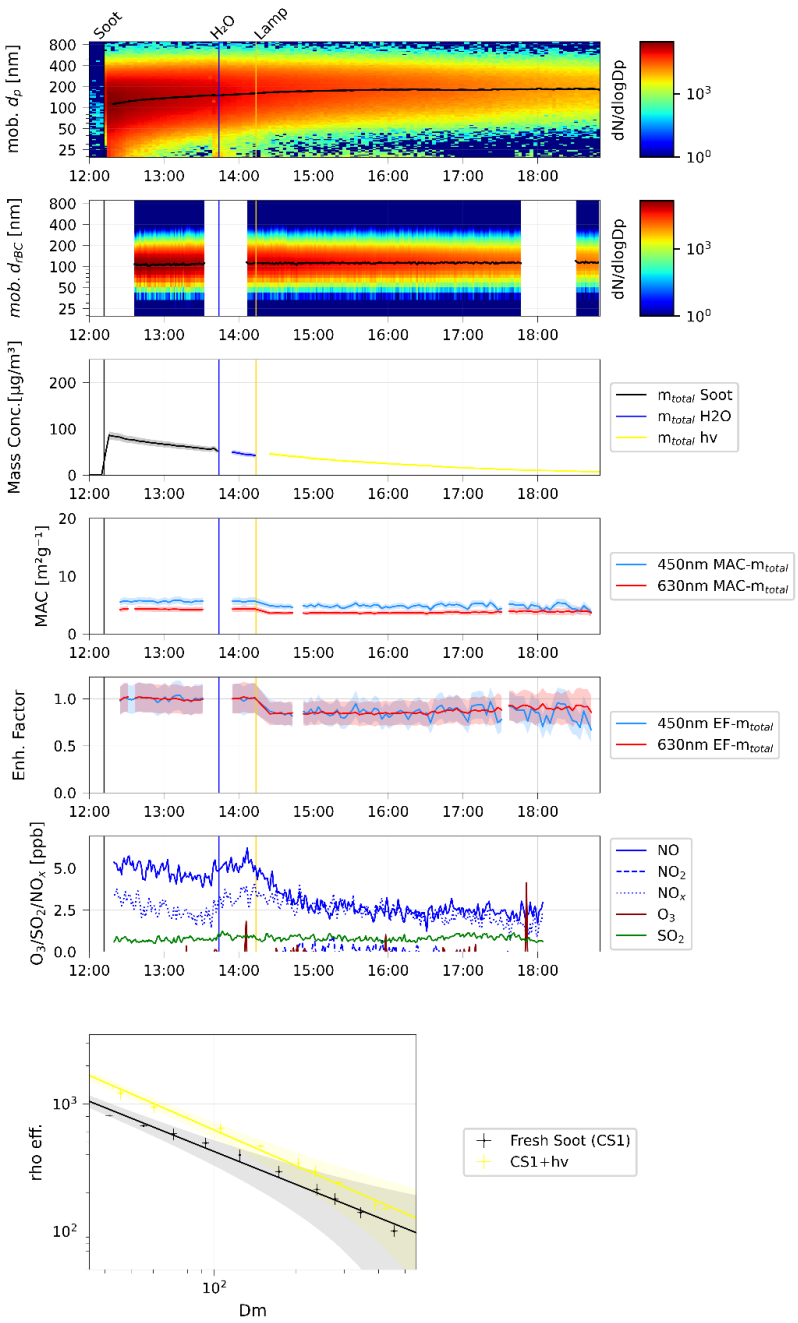
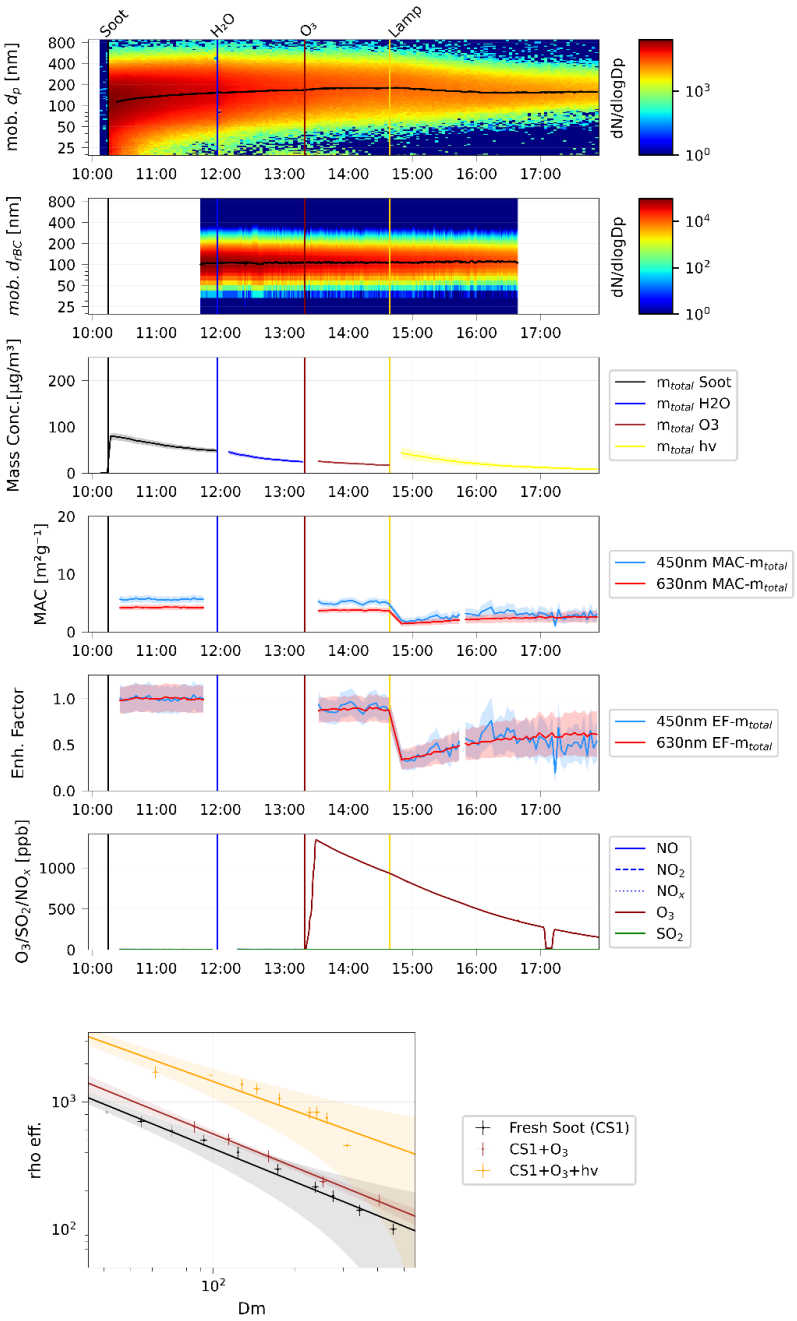


**Figure S23** Same as Fig. S11 for the CS1 $O_3$ irradiation humid experiment. To note that, differently from Fig. S11-S16, the MAC and EF values are here only calculated using $m_{total}$.



**Supplementary References**

Anderson, T. L., Covert, D. S., Marshall, S. F., Laucks, M. L., Charlson, R. J., Waggoner, A. P., Ogren, J. A., Caldow, R., Holm, R. L., Quant, F. R., Sem, G. J., Wiedensohler, A., Ahlquist, N. A., and Bates, T. S.: Performance Characteristics of a High-Sensitivity, Three-Wavelength, Total Scatter/Backscatter Nephelometer, J. Atmos. Oceanic Technol., 13, 967–986, https://doi.org/10.1175/1520-0426(1996)013%3C0967:PCOAHS%3E2.0.CO;2, 1996.

Bescond, A., Yon, J., Ouf, F. X., Ferry, D., Delhaye, D., Gaffié, D., Coppalle, A., and Rozé, C.: Automated Determination of Aggregate Primary Particle Size Distribution by TEM Image Analysis: Application to Soot, Aerosol Science and Technology, 48, 831–841, https://doi.org/10.1080/02786826.2014.932896, 2014.

Bond, T. C. and Bergstrom, R. W.: Light Absorption by Carbonaceous Particles: An Investigative Review, Aerosol Science and Technology, 40, 27–67, https://doi.org/10.1080/02786820500421521, 2006.

Dahneke, B.: Simple Kinetic Theory of Brownian Diffusion in Vapors and Aerosols, in: Theory of Dispersed Multiphase Flow, Elsevier, 97–133, https://doi.org/10.1016/B978-0-12-493120-6.50011-8, 1983.

DeCarlo, P. F., Slowik, J. G., Worsnop, D. R., Davidovits, P., and Jimenez, J. L.: Particle Morphology and Density Characterization by Combined Mobility and Aerodynamic Diameter Measurements. Part 1: Theory, Aerosol Science and Technology, 38, 1185–1205, https://doi.org/10.1080/027868290903907, 2004.

Denjean, C., Formenti, P., Picquet-Varrault, B., Pangui, E., Zapf, P., Katrib, Y., Giorio, C., Tapparo, A., Monod, A., Temime-Roussel, B., Decorse, P., Mangeney, C., and Doussin, J. F.: Relating hygroscopicity and optical properties to chemical composition and structure of secondary organic aerosol particles generated from the ozonolysis of α-pinene, Atmos. Chem. Phys., 15, 3339–3358, https://doi.org/10.5194/acp-15-3339-2015, 2015.

Fuchs, N. A., Daisley, R. E., Fuchs, M., Davies, C. N., and Straumanis, M. E.: *The Mechanics of Aerosols*, Physics Today, 18, 73–73, https://doi.org/10.1063/1.3047354, 1965.

Habib, Z. G. and Vervisch, P.: On The Refractive Index of Soot at Flame Temperature, Combustion Science and Technology, 59, 261–274, https://doi.org/10.1080/00102208808947100, 1988.

Heuser, J., Di Biagio, C., Yon, J., Cazaunau, M., Bergé, A., Pangui, E., Zanatta, M., Renzi, L., Marinoni, A., Inomata, S., Yu, C., Bernardoni, V., Chevaillier, S., Ferry, D., Laj, P., Maillé, M., Massabò, D., Mazzei, F., Noyalet, G., Tanimoto, H., Temime-Roussel, B., Vecchi, R., Vernocchi, V., Formenti, P., Picquet-Varrault, B., and Doussin, J.-F.: Spectral optical properties of soot: laboratory investigation of propane flame particles and their link to composition, Atmos. Chem. Phys., 25, 6407–6428, https://doi.org/10.5194/acp-25-6407-2025, 2025.

Kebabian, P. L., Robinson, W. A., and Freedman, A.: Optical extinction monitor using cw cavity enhanced detection, Review of Scientific Instruments, 78, 063102, https://doi.org/10.1063/1.2744223, 2007.

Kim, H., Barkey, B., and Paulson, S. E.: Real refractive indices of α- and β-pinene and toluene secondary organic aerosols generated from ozonolysis and photo-oxidation: REFRACTIVE INDICES OF ORGANIC AEROSOLS, J. Geophys. Res., 115, https://doi.org/10.1029/2010JD014549, 2010.

Laborde, M., Schnaiter, M., Linke, C., Saathoff, H., Naumann, K.-H., Möhler, O., Berlenz, S., Wagner, U., Taylor, J. W., Liu, D., Flynn, M., Allan, J. D., Coe, H., Heimerl, K., Dahlkötter, F., Weinzierl, B., Wollny, A. G., Zanatta, M., Cozic, J., Laj, P., Hitzenberger, R., Schwarz, J. P., and Gysel, M.: Single Particle Soot Photometer intercomparison at the AIDA chamber, Atmos. Meas. Tech., 5, 3077–3097, https://doi.org/10.5194/amt-5-3077-2012, 2012.

Massabò, D., Bernardoni, V., Bove, M. C., Brunengo, A., Cuccia, E., Piazzalunga, A., Prati, P., Valli, G., and Vecchi, R.: A multi-wavelength optical set-up for the characterization of carbonaceous particulate matter, Journal of Aerosol Science, 60, 34–46, https://doi.org/10.1016/j.jaerosci.2013.02.006, 2013.

Massoli, P., Murphy, D. M., Lack, D. A., Baynard, T., Brock, C. A., and Lovejoy, E. R.: Uncertainty in Light Scattering Measurements by TSI Nephelometer: Results from Laboratory Studies and Implications for Ambient Measurements, Aerosol Science and Technology, 43, 1064–1074, https://doi.org/10.1080/02786820903156542, 2009.

Massoli, P., Kebabian, P. L., Onasch, T. B., Hills, F. B., and Freedman, A.: Aerosol Light Extinction Measurements by Cavity Attenuated Phase Shift (CAPS) Spectroscopy: Laboratory Validation and Field Deployment of a Compact Aerosol Particle Extinction Monitor, Aerosol Science and Technology, 44, 428–435, https://doi.org/10.1080/02786821003716599, 2010.

Olfert, J. S. and Collings, N.: New method for particle mass classification—the Couette centrifugal particle mass analyzer, Journal of Aerosol Science, 36, 1338–1352, https://doi.org/10.1016/j.jaerosci.2005.03.006, 2005.

Onasch, T. B., Massoli, P., Kebabian, P. L., Hills, F. B., Bacon, F. W., and Freedman, A.: Single Scattering Albedo Monitor for Airborne Particulates, Aerosol Science and Technology, 49, 267–279, https://doi.org/10.1080/02786826.2015.1022248, 2015.

Otto, E. and Fissan, H.: Brownian coagulation of submicron particles, Advanced Powder Technology, 10, 1–20, https://doi.org/10.1016/S0921-8831(08)60453-7, 1999.

Otto, E., Fissan, H., Park, S. H., and Lee, K. W.: The log-normal size distribution theory of brownian aerosol coagulation for the entire particle size range, Journal of Aerosol Science, 30, 17–34, https://doi.org/10.1016/S0021-8502(98)00038-X, 1999.

Park, S. H., Lee, K. W., Otto, E., and Fissan, H.: The log-normal size distribution theory of brownian aerosol coagulation for the entire particle size range, Journal of Aerosol Science, 30, 3–16, https://doi.org/10.1016/S0021-8502(98)00037-8, 1999.

Petzold, A. and Schönlinner, M.: Multi-angle absorption photometry—a new method for the measurement of aerosol light absorption and atmospheric black carbon, Journal of Aerosol Science, 35, 421–441, https://doi.org/10.1016/j.jaerosci.2003.09.005, 2004.

Petzold, A., Schloesser, H., Sheridan, P. J., Arnott, W. P., Ogren, J. A., and Virkkula, A.: Evaluation of Multiangle Absorption Photometry for Measuring Aerosol Light Absorption, Aerosol Science and Technology, 39, 40–51, https://doi.org/10.1080/027868290901945, 2005.

Schnaiter, M., Linke, C., Möhler, O., Naumann, K. -H., Saathoff, H., Wagner, R., Schurath, U., and Wehner, B.: Absorption amplification of black carbon internally mixed with secondary organic aerosol, J. Geophys. Res., 110, 2005JD006046, https://doi.org/10.1029/2005JD006046, 2005.

Seinfeld, J. H. and Pandis, S. N.: Atmospheric chemistry and physics: from air pollution to climate change, Third edition., John Wiley & Sons, Hoboken, New Jersey, 1 pp., 2016.

Stephens, M., Turner, N., and Sandberg, J.: Particle identification by laser-induced incandescence in a solid-state laser cavity, Appl. Opt., 42, 3726, https://doi.org/10.1364/AO.42.003726, 2003.

Vecchi, R., Bernardoni, V., Paganelli, C., and Valli, G.: A filter-based light-absorption measurement with polar photometer: Effects of sampling artefacts from organic carbon, Journal of Aerosol Science, 70, 15–25, https://doi.org/10.1016/j.jaerosci.2013.12.012, 2014.

Yon, J., Bescond, A., and Ouf, F.-X.: A simple semi-empirical model for effective density measurements of fractal aggregates, Journal of Aerosol Science, 87, 28–37, https://doi.org/10.1016/j.jaerosci.2015.05.003, 2015.